UNIVERSITY OF CALIFORNIA, SAN DIEGO

Sensitivity analysis in multiscale, multi-physics problems

A dissertation submitted in partial satisfaction of the
requirements for the degree
Doctor of Philosophy

in

Materials Science and Engineering

by

Kimoon Um

Committee in charge:

Professor Daniel M. Tartakovsky, Co-Chair
Professor Prabhakar Bandaru, Co-Chair
Professor Shengquiang Cai
Professor Marcos Intaglietta
Professor Shankar Subramaniam

2018

The dissertation of Kimoon Um is approved, and

it is acceptable in quality and form for publication

on microfilm:

_____

_____

_____

_____
Co-Chair

_____
Co-Chair

University of California, San Diego

2018

DEDICATION

To “my family”

EPIGRAPH

Only the person who has faith in himself is able to be faithful to others.

—Erich Fromm

Impossible is just a big word thrown around by small men who find it easier to live in the world they've been given than to explore the power they have to change it. Impossible is not a fact. It's an opinion. Impossible is not a declaration. It's a dare. Impossible is potential. Impossible is temporary. Impossible is nothing

—Muhammad Ali

TABLE OF CONTENTS

LIST OF FIGURES

LIST OF TABLES

ACKNOWLEDGEMENTS

I would like to acknowledge Professor Daniel M. Tartakovsky for his endless support as my advisor and thoughtful advises as my friend during my doctoral period. His guidance has driven me to stay highly motivated all the time, has pointed me in the right direction, and has proved to be very invaluable. I also appreciate my family for their support and love. I can not describe their love with any existing word on the earth and they truly mean my presence.

The text of this dissertation includes reprints of the following papers, either published or accepted or submitted for consideration at the time of publication. The dissertation author was the primary investigator and author of these publications.

Chapter 2

Um, K. and D. M. Tartakovsky, "Hybrid models of chemotaxis with application to leukocyte migration", in preparation

Chapter 3

Um, K., X. Zhang, M. Katsoulakis, P. Plechac, and D. M. Tartakovsky, "Global sensitivity analysis of multiscale properties of porous materials", *Journal of Applied Physics*, 123, 075103 (2018).

Chapter 4

Um, K., E. Hall, M. Katsoulakis, and D. M. Tartakovsky, "Probabilistic graphical

models and multiscale porous media“, submitted

VITA

2018	Doctor of Philosophy in Materials Engineering and Science, University of California, San Diego
2006	Master of Science in Materials Engineering and Science, Seoul National University, Korea
2004	Bachelor of Science in Materials Engineering and Science, *cum laude*, Seoul National University, Korea

PUBLICATIONS

Um, K., X. Zhang, M. Katsoulakis, P. Plechac, and D. M. Tartakovsky, "Global sensitivity analysis of multiscale properties of porous materials", *Journal of Applied Physics*, 123, 075103 (2018).

Um, K. and D. M. Tartakovsky, "Hybrid models of chemotaxis with application to leukocyte migration", in preparation

Um, K., E. Hall, M. Katsoulakis, and D. M. Tartakovsky, "Probabilistic graphical models and multiscale porous media", submitted

Um, K., A. Salleo, and D. M. Tartakovsky, "Two-phase model of organic electochemical transistors", in preparation

ABSTRACT OF THE DISSERTATION

Sensitivity analysis in multiscale, multi-physics problems

by

Kimoon Um

Doctor of Philosophy in Materials Science and Engineering

University of California San Diego, 2018

Professor Daniel M. Tartakovsky, Co-Chair

Professor Prabhakar Bandaru, Co-Chair

This dissertation deals with multiscale and multi-physics mathematical modeling and global sensitivity analysis. Multiscale and multi-physics problems are ubiquitous in every field of science and engineering. For example, micro- or even nano-scale material properties often influence their large-scale properties, and microscopic interfaces between different materials affect bulk transport phenomena. We develop and deploy methods of global (variance-based) sensitivity analysis to determine how, and

to what degree, nano-scale characteristics of (nano)porous materials affect and give rise to bulk (Darcy-scale) properties.

We deploy stochastic multiscale algorithms to solve several problems of relevance in materials science and biology, and conduct rigorous sensitivity analysis and uncertainty quantification. In Chapter 2, we present a novel hybrid algorithm to ameliorate high computational costs typical of multiscale, multi-physics simulations, and apply it to solve a chemotaxis-diffusion-reaction problem. In Chapter 3, we report on our pore- and multi-scale simulations and perform a global (variance-based) sensitivity analysis for uncorrelated input parameters. This chapter also contains results of our uncertainty quantification analysis for this multiscale problem, which is based on a (generalized) polynomial chaos expansion (gPCE). This UQ strategy can be used to identify a set of pore-scale characteristics for robust materials design. In Chapter 4, we introduce a novel graph-theoretic approach to conduct global sensitivity analyses in the presence of correlated inputs.

Chapter 1

Introduction

Many physical problems of current interest are complex in nature, and composed of separate physical phenomena. Each constituent phenomenon can reinforce or dampen another, giving rise to rich and sometimes unexpected behavior. Various physical and/or (bio)chemical sub-models can take place and operate either at the same or vastly different spatiotemporal scales. To understand a system's behavior, it is often necessary to capture both the behavior of individual components and their interactions and cross-communication. Multiphysics plays an equally strong role is the design of subsystems and how they interact with other subsystems and systems. One example is MEMS (microelectromechanical systems), which typically include small moving parts such as wheels, rotors, levers and linkages, that are integrated into a larger system. Other examples include the creation of "designer materials" tailored for specific envi-

ronments, as well as the simulation of nano-scale mechanics of white blood cells and how that is being transported to inflammation location for medical treatment devices and methods.

Multiscale nature of many phenomena poses another complication. For example, small-scale (micro- or nano-scale) properties often influence bulk material properties (i.e., on the continuum or Darcy scale). Engineers often need to simulate large-scale structures in which micro-mechanical properties of constituent materials greatly affect the overall behavior of the system. As such, the micro-structure and mechanical properties need to be introduced explicitly in the analysis procedure. Multiscale and multi-physics models are different but share many common features since both need coupling strategies to combine their constitutive sub-models.

When using traditional single-scale simulation methods such as FDM (Finite Difference Method), FVM (Finite Volume method), FEA (Finite Elements Analysis), even modern computers are pushed to their limits in trying to resolve all the relevant details of multiscale systems. This fact necessitates the development of hybrid methods, which couple micro- and macros-scale models and simulation. Our focus is on identifying and capturing key multiscale features of several diverse problems of practical significance, and on identifying channels through which parametric uncertainty propagates through scales.

1.1 Discrete and continuum multiscale simulations

Many biological process on sub-cellular level involve species whose numbers vary by many orders of magnitude. If a small number of molecules/agents is present in a system, their apparent behavior becomes random and exhibit spatiotemporal fluctuations which can be captured by stochastic simulation. On the other hand, such molecules/agents typically interact with other species whose concentrations (numbers of molecules per unit volume) are many, many orders of magnitude higher. Simulation of such systems is notoriously difficult and increasingly relies on multiscale hybrid methods, which combine continuum-scale (deterministic) descriptors of reacting species with large numbers of molecules/agents and discrete (stochastic) descriptors of reacting species with small numbers of molecules/agents. For example, chemo-attractants (some of the chemicals involved in inflammation) diffuse through the tissue at concentrations that far exceed the numbers of bacteria or leukocytes present. The process by which leukocytes (randomly) move towards a wound surrounded by bacteria is called chemotaxis. We develop and implement numerically a novel hybrid algorithm that captures the random motion of leukocytes and relies on discrete/continuous representations of chemotaxis(advection)-motility(diffusion)-reaction phenomena. This motion is affected and "guided" by the concentration of chemo-attractants, whose gradients are computed at the continuum scale to determine chemotactic velocity. Leukocyte

motility and reactions described by Brownian motion and stochastic simulation algorithm, respectively. We develop a hybrid algorithm, which bridges these two scales and captures the complexity of biochemical processes and the wide range of concentrations. Time step is chosen by comparing the Péclet number and the Damköhler number at every simulation step. We deploy our algorithm in three case studies. In the first, we verify our hybrid algorithm by comparing its predictions for large numbers of all the reactants involved (i.e., for a situation where randomness is expected to play minor role in system's dynamics) with an analytical solution of chemotaxis(advection)-motility(diffusion) equations for several Pécelt numbers. The second case study involves a small number of leukocytes and serves to highlight the effects of randomness in an inflammation process described, alternatively, by one-dimensional chemotaxis-motility-reaction equations on the continuum scale and by our hybrid model. In the third case study, we construct a more realistic two-dimensional model, in leukocytes randomly move from the skin to a capillary.

1.2 Multiscale simulations with independent and correlated inputs

Ubiquitous uncertainty about pore geometry inevitably undermines the veracity of pore- and multi-scale simulations of transport phenomena in porous media. It raises

two fundamental issues: sensitivity of effective material properties to pore-scale parameters and statistical parameterization of Darcy-scale models that accounts for pore-scale uncertainty. Homogenization-based maps of pore-scale parameters onto their Darcy-scale counterparts facilitate both sensitivity analysis (SA) and uncertainty quantification. We treat uncertain geometric characteristics of a hierarchical porous medium as random variables to conduct global SA and to derive probabilistic descriptors of effective diffusion coefficients and effective sorption rate. Our analysis is formulated in terms of solute transport diffusing through a fluid-filled pore space, while sorbing to the solid matrix. Yet it is sufficiently general to be applied to other multiscale porous media phenomena that are amenable to homogenization.

Such analyses treat input parameters (coefficients) as mutually uncorrelated, and are generally valid for a small range of correlated inputs as ab approximation. As the ranges over which input parameters are allowed to vary become larger, the nonlinear relationships between various pore-geometry parameters significantly complicates the global (variance-based) sensitivity analysis. We handle the inter-dependence between input parameters by developing a probabilistic graphical method.

1.3 Dissertation content

My research consists of four inter-related components, each of which is presented in a separate chapter. In Chapter 2, we present a novel hybrid algorithm to ameliorate high computational costs typical of multiscale, multi-physics simulations, and apply it to solve a chemotaxis-diffusion-reaction problem.

In Chapter 3, we report on our pore- and multi-scale simulations and perform a global (variance-based) sensitivity analysis for uncorrelated input parameters. This chapter also contains results of our uncertainty quantification analysis for this multi-scale problem, which is based on a (generalized) polynomial chaos expansion (gPCE). This UQ strategy can be used to identify a set of pore-scale characteristics for robust materials design.

In Chapter 4, we introduce a novel graph-theoretic approach to conduct global sensitivity analyses in the presence of correlated inputs.

Chapter 2

Hybrid method of multi-scale model in chemotaxis-motility-reaction system

Two mathematical frameworks, discrete and continuous, are routinely used to model kinetics of complex (bio)chemical systems. The first framework is based on the chemical master equation[1, 2]; it is invoked when the number of molecules of reacting species is relatively small, so that stochastic fluctuations in local concentrations become pronounced. This randomness is a key feature of many biological processes, e.g., gene

expression[3]. The second framework consists of differential equations describing temporal evolution of species concentrations; it predicts average behavior of large numbers of molecules. Both frameworks can handle spatial variability, e.g., by adopting operator splitting techniques for discrete reaction-diffusion processes[4] or partial-differential equations (PDEs) for their continuous counterparts.

Many systems involve reacting species with vastly different number of molecules/ agents, thus necessitating the simultaneous use of discrete and continuous descriptors, i.e., call for the use of hybrid simulations. This occurs when a PDE-based model for one or more species fails either locally, in a (small) part of a computational domain[5, 6], or globally, over the whole simulation domain[7]. These two types of hybrid simulations differ in the way they couple their discrete and continuous components. We focus on the latter class of phenomena, of which leukocyte migration towards a pathogen is a pertinent example.

Leukocytes, or white blood cells, are instrumental in a body's immune response to invading pathogens, such as bacteria, viruses, or parasites. A pathogen-induced inflammation activates leukocytes in the bloodstream, causing their transmigration from blood vessels to the surrounding tissue. Within the affected tissue leukocytes move towards a contaminated site, exhibiting undirected (diffusion-like) and directed (chemotaxis) forms of motion as well as interacting with a pathogen. Continuum-level representations of the latter stage of leukocyte migration rely on systems of coupled

PDEs of various degrees of complexity, ranging from the celebrated Keller-Segel chemotaxis model[8] to its more evolved counterparts[9]. Such models track concentrations of relevant species—the concentrations of leukocytes, $\mathcal{C}(\mathbf{x}, t)$, and chemoattractant, $\mathcal{A}(\mathbf{x}, t)$, in the Keller-Segel model[8]—in space, $\mathbf{x}$, and time, t. While large numbers of chemoattractant molecules justify the use of a PDE-based model to describe the spatiotemporal evolution of $\mathcal{A}(\mathbf{x}, t)$, small numbers of leukocytes and bacteria involved in the process render such continuum treatments problematic. Taken in isolation, a motion of individual leukocytes has been described by, e.g., biased random walk[10, 11].

We present a hybrid algorithm that combines a continuum description of chemoattractants with discrete representations of leukocytes and bacteria. We provides a mathematical model of leukocyte migration towards an inflammation site, including its continuum (PDE-based) formulation. Our hybrid method and its algorithmic implementation are presented in Section 2.1. They are used in Section 2.2 to solve three problems of increasing complexity. The first, a one-dimensional advection-diffusion equation, serves to verify our algorithm by comparing its predictions with an analytical solution and to analyze the effect of a finite number of particles on the adequacy of the continuum model. The second, unidirectional leukocyte migration in the presence of chemoattractant and bacteria, accomplishes the same goals by comparing our predictions with those provided by solving numerically a system of one-dimensional chemotaxis-motility-reaction PDEs. The third problem deals with a more realistic

two-dimensional setting, which represents leukocyte migration towards a wound. Main conclusions drawn from our study are summarized in Section 2.3.

2.1 METHOD

Small(Finite) number of molecules compared with large number of inducing molecules invoke the need of hybrid model based on particle method, stochastic simulation by transferring Eq.(2.25a) $\sim$ Eq.(2.26) into the discrete model. In chemotaxis-motility-reaction sytem, chemo-attractants are inducing molecules and computed in the continuum scale using mesh-based PDE model though bacteria and leukocytes are solved by discrete model. Number of bacteria in each mesh element has effect on the chemo-attractants and chemotaxis velocity of leukocyte is determined by the concentration and the concentration gradient of chemo-attractants where leukocytes are located. Position of each bacteria molecule and leukocytes molecule is updated by the random motility(μ_b or μ) and/or by the chemotaxis velocity. Bacteria and leukocytes react when they are close and collide each other.

2.1.1 Stochastic method

In the deterministic chemotaxis-motility-reaction systems of continuum model, different time scale among three phenomenon makes operator splitting applied. Chemo-

taxis and motility are solved explicitly and (stiff) reaction is solved implicitly [12].

The reaction-diffusion system using stochastic method [4] is modified in our hybrid method because of chemotaxis. Two different pheonomenons, chemotaxis-motility and reaction are calculated separately. In our system, bacteria undergo reaction-diffusion system though leukocytes do chemotaxis(advection) – motility(diffusion) – reaction. Chemotaxis is solved using chemo-attractants' concentration and gradient of chemo-attractant and motility is solved using Brownian motion. And (modified) Gillespie method is utilized to solve reaction assuming that bacteria and leuckocytes are well-mixed in a same mesh-element.

Operator splitting method

Operator splitting algotithm [13] to leukocytes chemotaxis-motility-reaction is

$$\frac{\partial \mathcal{C}'}{\partial t} = -\nabla \mathbf{J} = \mu \nabla^2 \mathcal{C}' - \nabla \cdot (\mathbf{V_c} \mathcal{C}') \tag{2.1a}$$

$$\frac{\partial \mathcal{C}''}{\partial t} = -(g_0 + g_1 \mathcal{B}'') \mathcal{C}'' \tag{2.1b}$$

during the time interval $[t, t + \Delta t]$. Here $\mathcal{C}'(t) = \mathcal{C}(t)$ and $\mathcal{C}''(t) = \mathcal{C}'(t + \Delta t)$, so that $\mathcal{C}''(t) = \mathcal{C}(t + \Delta t)$. Compute the position of i–th cell of j–th kind($j = 1$ for bacteria and $j = 2$ for leukocytes) at time $t + \Delta t$ as

$$\mathbf{X}_i^j(t + \Delta t) = \mathbf{X}_i^j(t) - \mathbf{V}_i^j \Delta t + \sqrt{2\mu_j \Delta t}\boldsymbol{\xi} \tag{2.2}$$

where Δt is time step to update new position. $\mathbf{V_c}$ is the chemotactic velocity vector in each direction only for leukocytes, which is $\mathbf{V_c} = \mathbf{V_c}(a, \Delta a)$. $\boldsymbol{\xi}$ is a vector of random variables with normal distributed in each direction to represent Brownian motion.

And we assume that bacteria and leukocytes are well-mixed states and they undergo reaction process by Gillespie method in Eq.(2.5)–Eq.(2.6).

Stochastic Simulation Algorithm : Reaction

Bacteria($\mathcal{B}$) in the wound site is reproduced with the growth rate, k_g, leukocyte($\mathcal{C}$) is died with the natural dying rate, g_0 We assumed bacteria and leukocyte died at the same rate of k_d and g_1.

$$\mathcal{B} \xrightarrow{kg} 2\mathcal{B}, \qquad \mathcal{C} \xrightarrow{g_0} \phi, \qquad \mathcal{B} + \mathcal{C} \xrightarrow{k_d(=g_1)} \phi \tag{2.3}$$

The reaction between bacteria and leukocyte needs no activation energy (diffusion-controlled reaction) within effective radius $(r_a + r_b)$ and the reaction rate constant k_d is

$$k_d = 4\pi(\mu_b + \mu)(r_b + r_c) \times Avo \times 10^3 \tag{2.4}$$

where μ_b and μ are the motility coefficient of bacteria and leukocyte. And r_b and r_c are radius of theirs. Avo is the Avogadro's number. Reaction between the concentration of bacteria($\mathcal{B}$) and that of leukocyte($\mathcal{C}$) is implicitly solved by the Newton-Raphson method.

Gillespie multi-particle (GMP) method [14] is one of most popular method to solve chemical reaction with diffusion. But we implement Brownian dynamics instead of cellular automata and stochastic simulation analysis(SSA) due to better accuracy. We discretize our domain into m cells and assumed that bacteria particles and leukocyte particles were well-distributed within a cell. k–th cell ($k = 1, \cdots, m$) has n_b^k bacteria cells and n_c^k leukocytes cells respectively. Two random variables, r_1 and r_2 are uniformly distributed in [0, 1]. The continuous random value τ_{R_k} is reaction time step within Δt.

$$\tau_{R_k} = \frac{1}{a_{\text{sum}}^k} \ln\left(\frac{1}{r_1}\right) = \frac{-\ln r_1}{a_{\text{sum}}^k},$$
$$\sum_{j'=1}^{j-1} a_{j'} \leq r_2 a_{\text{sum}}^k \leq \sum_{j'=1}^{j} a_{j'} \tag{2.5}$$

where a_{sum} is the sum of all propensity functions(a_j). After reaction time (τ_{R_k}) process, the system state, $\boldsymbol{n}$, at time $t + \tau_{R_k}$ is

$$\boldsymbol{n}(t + \tau_{R_k}) = \boldsymbol{n}(t) + \boldsymbol{\nu}_k, \tag{2.6}$$

where $\boldsymbol{\nu}_k = (\Delta n_b^k, \Delta n_c^k)^T$.

Brownian Dynamics : Random motility

The population of bacteria or leukocytes is considered as random motility with single-cell parameters(μ_b, μ respectively) [15], which acts as the diffusion coefficient of single particle movement in our model.

$$\mu = \frac{1}{2} T_p v^2, \tag{2.7}$$

where T_p is persistence time which is the time period before cell changing direction, and v is its maximum velocity. Random motility of bacteria, μ_b, is very small and set as $10^{-15}\, m^2/s$.

Brownian dynamics of bacteria and leukocytes in our method is applied as random walk with the motility[16]. Motility of bacteria in stochastic equation is

$$X^B(t + \Delta t) = X^B(t) + \sqrt{2\mu_b \Delta t}\boldsymbol{\xi}, \tag{2.8}$$

where Δt is the time step, ξ is a standard Gaussian random variable and μ_b is the random motility of bacteria.

Chemotaxis

Chemotaxis coefficient, χ is computed as

$$\chi = v\frac{\chi_0 \frac{\partial N_b}{\partial \mathcal{A}}}{1 + \chi_0 \frac{\partial N_b}{\partial \mathcal{A}} \frac{\partial \mathcal{A}}{\partial x}}, \tag{2.9}$$

where v is the maximum velocity of a leukocyte. Chemotactic belocity V_c is characterized by chemotaxis coefficient χ and the gradient of $\mathcal{A}$. And we define the oriental bias, $\boldsymbol{\phi}$, which varies from 0 (purely random motility) to 1 (full oriented motility)[17][18].

$$V_c(\mathcal{A}, \Delta\mathcal{A}) = \chi\frac{\partial A}{\partial x} = v\phi = v\frac{\chi_0 \frac{\partial N_b}{\partial \mathcal{A}} \frac{\partial \mathcal{A}}{\partial x}}{1 + \chi_0 \frac{\partial N_b}{\partial \mathcal{A}} \frac{\partial \mathcal{A}}{\partial x}} \tag{2.10}$$

where χ_0 is chemotactic sensitivity, N_b is the number of bound receptors on the cell membrane. And N_b is related to concentration of chemo-attractant $\mathcal{A}(\mathbf{x}, t)$ by

Michaelis-Menten relationship

$$N_b = \frac{N_T \mathcal{A}}{K_d + \mathcal{A}} \tag{2.11}$$

where N_T is the total number of cell receptors on the cell membrane and K_d is the receptor dissociation constant.

And the stochastic equation of a leukocyte is

$$X^C(t + \Delta t) = X^C(t) + V_c \Delta t + \sqrt{2\mu\Delta t}\boldsymbol{\xi}, \tag{2.12}$$

where V_c is the chemotactic velocity and calculated from Eq.(2.10).

Initial and boundary condition

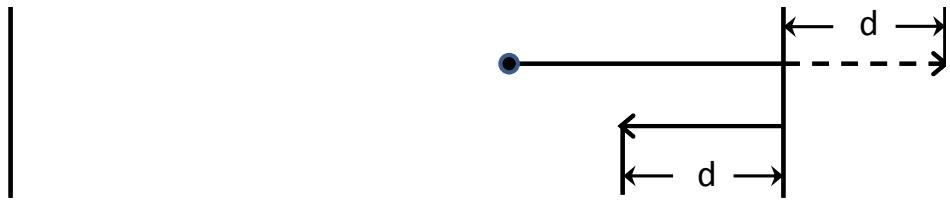

Figure 2.1: Schematic view of reflective boundary. Vertical lines : the location of each boundary, Solid circle : starting location of particle, Horizontal solid line : trajectories within the domain, and Dashed line : the trace after reflecting the boundary.

In our method, the initial condition of bacteria and luekoyctes, Eq.(2.29)–Eq.(2.30) are transferred as initial number of each cell and they have the reflective boundary condition.

$$X^B(t_0) = \mathcal{F}_x, \quad \mathcal{F}_x = N_0^B \delta(x - (x_s + \epsilon)), \tag{2.13}$$

$$X^C(t_0) = \mathcal{G}_x, \quad \mathcal{G}_x = N_0^C \delta(x - (x_f - \epsilon)), \tag{2.14}$$

where N_0^B and N_0^C are the initial number of bacteria and leukocytes respectively at the very small distance from the each boundaries which represent the skin surface and the blood vessel. The reflective boundary which is in accordance with no flux boundary is depicted in Fig.2.1. And the reflective boundary is assumed that there is a barrier at the boundary which rebounds cells into domain with perfectly elastic collision. This causes opposite direction of velocity with the same magnitude and no change for other properties[19].

2.1.2 Continuum method : Chemo-attractants

Chemo-attractants behave continuous motion of diffusion and are produced by bacteria. Relatively high concentration against the bacteria and the leukocytes brings about continuum scale calculation to solve diffusion and reaction for chemo-attractants. Implicit-Explicit method(IMEX) based on Finite Volume Method(FVM) is implemented to obtain the concentration distribution of chemo-attractants, which is described in 2.1.2. The concentration profile of chemo-attractants plays a key role as determining the chemotactic velocity of leukocytes explained in Section 2.1.1, which move toward higher concentration sites of chemo-attractants, the wound site.

The discretization in time and space of Eq.(2.34) in (i, j)–th element at $n + 1$

time step is

$$\frac{\mathcal{A}_{i,j}^{n+1}-\mathcal{A}_{i,j}^{n}}{\Delta t}=D\Big(\frac{\mathcal{A}_{i+1,j}^{n+1}-2a_{i,j}^{n+1}-\mathcal{A}_{i-1,j}^{n+1}}{\Delta x^2} + \frac{\mathcal{A}_{i,j+1}^{n+1}-2\mathcal{A}_{i,j}^{n+1}-\mathcal{A}_{i,j-1}^{n+1}}{\Delta y^2}\Big)+k_p b_{i,j}^{n} \tag{2.15a}$$

$$-s_y\mathcal{A}_{i,j-1}^{n+1}-s_x\mathcal{A}_{i-1,j}^{n+1}+(1+2s_x+2s_y)\mathcal{A}_{i,j}^{n+1} -s_x\mathcal{A}_{i+1,j}^{n+1}-s_y\mathcal{A}_{i,j+1}^{n+1}=\Delta t\mathcal{A}_{i,j}^{n}+\Delta t k_p b_{i,j}^{n} \tag{2.15b}$$

where $s_x=\frac{D\Delta t}{\Delta x^2}$ and $s_y=\frac{D\Delta t}{\Delta y^2}$. Timestep Δt is varied at every timestep, which is explained in Section 2.1.3. This discretization is composed of penta-diagonal matrix and is solved by using the restarted Generalized Minimum Residual (GMRES) algorithm [20].

2.1.3 Time-step Decision

The proper time step is determined by considering chemotaxis, random motility and reaction of leukocytes in every time step. First, time step comes from leukocytes's migration (random motility and chemotaxis) which chracterized by Pèclet number

$$Pe=\frac{V_C h_{min}}{\mu}=\frac{\tau_D}{\tau_C} \tag{2.16}$$

where h_{min} is the smallest element-mesh size, and τ_D and τ_C represent different time scales for random motility and chemotaxis respectively. Diffusion-dominated($Pe<1$) or advection-dominated($Pe>1$) regime is determined by Pèclet number. We keep smaller time step between τ_C and τ_D as the drift time step, τ_{DR} and make comparison

this with the reaction time step.

$$\tau_{DR} = \min\{\tau_D, \tau_C\} \tag{2.17}$$

Reaction time step is the minimum of all k-th leukocyte cell from Eq.(2.5)

$$T_{R_k} = \frac{1}{a^k_{\text{sum}}}, \qquad a^k_{\text{sum}} \equiv \sum_{j=1}^{N} a_j(\mathbf{X}_k) \tag{2.18}$$

where $\boldsymbol{X}_k$ is the state of $\boldsymbol{X}$ of k–th leukocytes molecule and $a_j(\boldsymbol{X}_k)$ is the propensity function for j–th reaction. We set up the minimum time step at each time step out of whole domain.

$$T_R^{\min} \equiv \min T_{R_k}, \quad \text{where } k = 1, \cdots, m \tag{2.19}$$

And its reaction time step is considered with the Damköhler number

$$Da = \frac{\tau_{DR}}{T_R^{\min}}, \qquad \text{where } \tau_{DR} = \min(\tau_C, \tau_D) \tag{2.20}$$

Drift time step, τ_{DR} is minimum time during leukocytes' migration between chemotaxis and random motility.

We determine time step whether our model is reaction-controlled ($Da >> 1$) or drift-controlled($Da < 1$) regime at each time step considering the Damköhler number. This system would be homogenized well under drift-controlled regime which secures time of reaction and we choose the time step as the drift time($\Delta t_{step} = \tau_{DR}$). If our system is reaction-controlled regime, we should choose more time step size rather than $\Delta t_{step} = T_R^{min}$ considering small number of the bacteria molecule and the leukocytes

molecule where it has reaction, or high speed of leukocyte around the source of chemo-attractants. We set $\Delta t_{step} = 5\tau_{DR}$ with $0.5 < Da < 1.0$ and $\Delta t_{step} = 10\tau_{DR}$ with $Da < 0.5$ to procure enough reaction time[4] of firing reaction between bacteria and leukocytes.

2.1.4 Algorithm

A detailed algorithm for the applied numerical method suggested above is shown below.

---

1. For a given space dimension d and cell size $\Delta\mathbf{x}$, calculate the diffusion time step $\tau_{D_i} = \min\{\Delta\mathbf{x}\}/(2D_i d)$ of diffusing species $i = 1, \cdots, M$ and let $\tau_D = \min\{\tau_{D_i}\}$.

2. Initialize $t = t_i$

3. *While* $t \leq t_f$

   (a) Define whether system is drift- or reaction-controlled at every time step.

      i. Calculate τ_{DR} through Eq.(2.16)

         - Calculate the distribution of chemo-attractant using the expected time step. Use previous time step but diffusion time step for the first time step.

- Calculate the chemotactic velocity of every leukocyte through Eq. (2.10) for Pe

ii. Calculate $T_R^{\min}$ through Eq.(2.19)

iii. Calculate time step, Δt_{step} considering Da

(b) Let $t_{old} = t$

(c) Perform the drift step(Diffusion-Chemotaxis) and the reaction step using operator-splitting method.

i. Drift step with time-step Δt_{step}

- Chemo-attractants diffusion-reaction using IMEX
- Diffusion for bacteria and leukocytes using Brownian dynamics to advance.
- Chemotaxis using the calculated chemotactic velocity to advance species.

ii. Reaction step for each cell

- *While* $(t - t_{old}) \leq \Delta t_{step}$

  Calculate reaction time step τ_R using Eq.(2.5) within Δt_{step}.

  - If $\tau_R \leq \Delta t_{step}$, update the state vector through Eq.(2.6)

  - Otherwise, do not update the state vector

end *while*

iii. Go to next cell to calculate reaction

(d) Let $t = t_{old} + \Delta t_{step}$ for all cells

end *while*

2.2 RESULTS

Hybrid method is studied in one dimensional case and two dimensional case. In one dimension case, analytic solution and stochastic solution in advection-diffusion are compared in various Pèclet number in 2.2.1 and show our method fits well. In 2.2.2, relatively large number of leukocytes cells and bacteria cells are applied and the results of chemotaxis-motility-reaction are compared with continuum scale by normalizing the initial input number of them. Continuum method fails when applied small concentration but hybrid method shows better result with the small number of cells(or small concentration) in the view of calculation time. We show more realistic case study in two dimension case by domain size from the skin to capillary vessel (about $1\,mm$) and multi-site input points of leukocytes at the capillary in section 2.2.3.

We solve random motility(diffusion)-chemotaxis(advection) using TVD (2nd order) [21] for chemotaxis and reaction using Netwon Raphson method in continnum scale [22]. Though Eq.(2.8)–Eq.(2.12) are used to calculate position of bacteria and

leukocytes and Eq.(2.5)–Eq.(2.6) are used for reaction in hybrid method. Parameters are reported in TABLE 2.2.

2.2.1 Comparison between analytic solution and stochastic solution for Diffusion-Advection

Comparison of the deterministic solution and stochastic solution is shown semi-infinte domain, $\Omega \in [0\,\infty]$. Deterministic solutions have a Dirac delta type point source as an initial condition and no flux boundary condition at $x = 0$ and goes to zero at infinite domain.

$$\frac{\partial u}{\partial t} + v\frac{\partial u}{\partial x} = D\frac{\partial^2 u}{\partial x^2}, \quad x \in [0,\ \infty], \tag{2.21}$$

$$\text{IC: } u(x, t_0) = \delta_0(x),$$

$$\text{BCs: } u(0,t) + D\frac{\partial u(0,t)}{\partial t} = 0, \quad u(\infty, t) = 0$$

We transfer continuum equation of advection-diffusion equation(Eq.(2.21) into stochastic equation which has a reflective boundary condition(2.1) at $x = 0$ and make particles locate very close to this boundary at $t = 0s$ for n particles. The position of each particles are described with Brownian dynamics and are transferred with velocity,

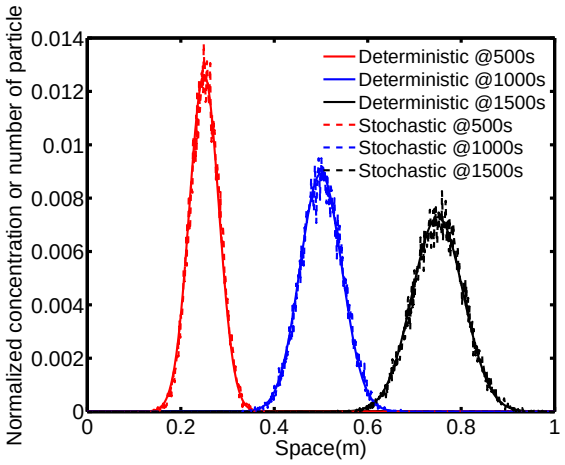

(a) $Pe = 0.5$

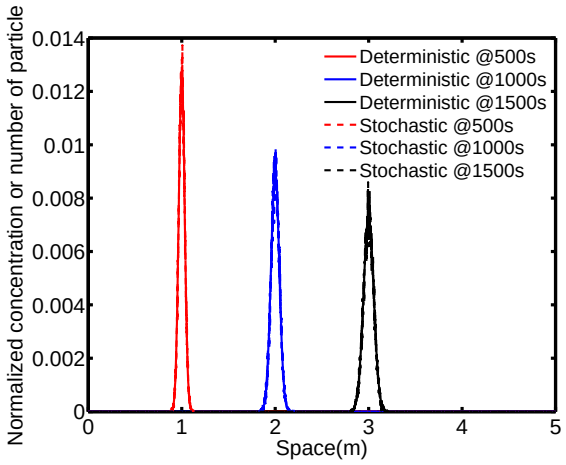

(b) $Pe = 2.0$

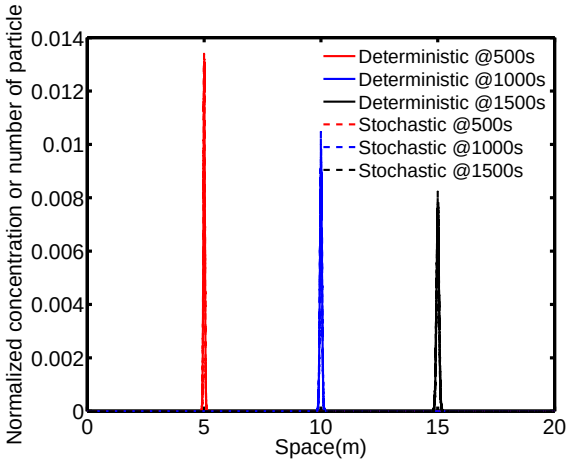

(c) $Pe = 10$

Figure 2.2: Deterministic solutions have Dirac-delta type point source and stochastic solutions are normalized with initial number of paticles. Results are shown at $t = 500s$, $t = 1000s$, and $t = 1500s$ with different Pèclet numbers.

v.

$$C^i(t+\Delta t) = C^i(t) + \sqrt{2D\Delta t}\xi + v\Delta t \tag{2.22}$$

$$C^i(0) = \epsilon, \quad \text{where } \epsilon \ll 1$$

where $i = 1, \cdots, n$. Diffusion coefficient, D is $10^{-5}m^2/s$ and the velocity, v is varied to see whether it is diffusion-dominated or advection-dominated and set cell Pèclet numbers as

$$Pe = \frac{v\Delta x}{D}. \tag{2.23}$$

The cell Pèclet number represents diffusion-dominated($Pe < 1$),

and advection-dominated($Pe \gg 1$). 0.5, 2.0, and 10.0.

The comparison results between analytic solution and stochastic solution i shown in figure 2.2. We use 10000 particles to compare the results with analytic solution. Our method using Brownian Dynamics and explicit velocity update works well. We set $\Delta x = 0.01m$ and normalize number of particles in each cell with total number of initial particles. Our method works well regardless Pèclet number.

The error is analyzed with L_2–Norm with respect to number of total input particles.

$$L_2\text{–Norm} = \sqrt{\sum_{i=1}^{n}(c(i) - C(i)^2)} \tag{2.24}$$

where $c(i)$ is analytic solution at $x = (i - 0.5)\Delta x$ and $C(i)$ is normalized number of particles at i–th cell which is $(i-1)\Delta x \leq x \leq i\Delta x$. Our method is not related to cell

size directly but it is neccessary to set up cell size to count number of particles inside.

The error decreases with increasing the number of particles shown in figure 2.3. We take L_2–Norms for five realizations and take the average values for different number of particles such as $2^p \times 1000$ where $p = 1, 2, ..., 8$.

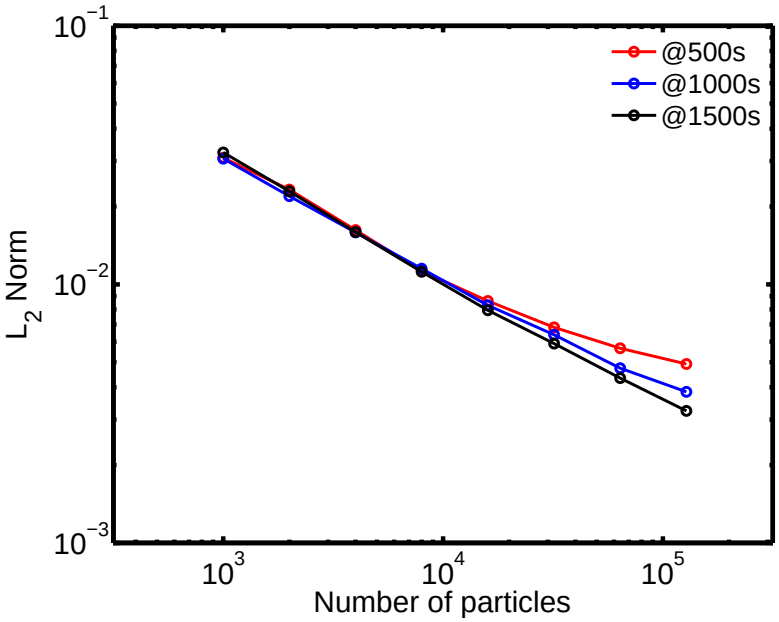

Figure 2.3: Error Analysis at $t = 500s$, $t = 1000s$, and $t = 1500s$: L_2–Norms are shown in log–log scale when number of particles are 1000, 2000, 4000, 8000, 16000, 32000, 64000, and 128000

2.2.2 Hybrid method results in one dimensional behavior

Here we are interested in the chemotactic behavior of leukocytes caused by the distribution of chemo-attractants and the reaction between the bacteria and leukocytes. Keller and Segel [8] considered a 1-D spatial domain as $\Omega \in [x_s,\ x_f] = [0,\ 10^{-3}m]$ and a time domain as $T \in [t_0, t_f] = [0,\ 3000s]$. Let $\mathcal{C}(x,t)$ denote the concentration of

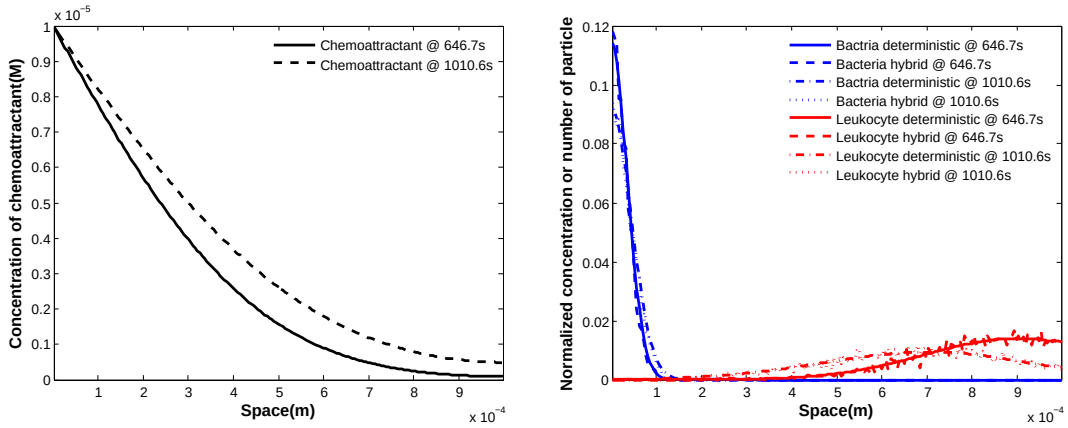

(a) Chemo-attractant (b) Bacteria and Leukocyte

Figure 2.4: Results in 1D simulation at $t = 646.7s$ and $t = 1010.6s$; (a) Chemo-attractants concentration (b) Bacteria and leukocyte in normalized value with respect to initial values. Solid line : continuum scale, Dash-dot : hybrid-method.

the leukocytes, $\mathcal{B}(x,t)$ the concentration of bacteria, and $\mathcal{A}(x,t)$ the concentration of chemo-attractants. Leukocytes move toward higher concentration of chemo-attractant through chemotaxis. It naturally dies and is degraded with contact to bacteria after digesting it.

$$\frac{\partial \mathcal{C}(x,t)}{\partial t} = -\frac{\partial J_c(x,t)}{\partial x} - (g_0 - g_1 \mathcal{B}(x,t))\mathcal{C}(x,t), \tag{2.25a}$$

$$J_c(x,t) = -\mu \frac{\mathcal{C}(x,t)}{\partial x} + \mathcal{C}(x,t)\chi \frac{\partial \mathcal{A}(x,t)}{\partial x}, \tag{2.25b}$$

where μ is the random motility coefficient of leukocytes and χ is the chemotaxis coefficient related to the strength and the gradient of concentration of chemo-attractants. They are removed by the natural death with the rate of g_0 and by the interaction with bacteria with the rate of g_1 in the cell. We assume the interaction rates between bacteria and leukocytes, which k_d and g_1 are the same.

Bacteria randomly move in the cell. They reproduce and are removed if they are caught by leukocytes.

$$\frac{\partial \mathcal{B}(x,t)}{\partial t} = \mu_b \frac{\partial^2 \mathcal{B}(x,t)}{\partial x^2} + (k_g - k_d \mathcal{C}(x,t))\mathcal{B}(x,t), \tag{2.26}$$

where μ_b is random motility coefficient of bacteria. k_g and k_d are respectively the growth rate and the consumption rate of bacteria when they meet leukocytes.

Chemo-attractants diffuse into cell at the wound site and is produced by the result of bacteria metabolism.

$$\frac{\partial \mathcal{A}(x,t)}{\partial t} = D \frac{\partial^2 \mathcal{A}(x,t)}{\partial x^2} + k_p \mathcal{B}(x,t), \tag{2.27}$$

where D is the diffusion coefficient and k_p is the rate of production.

Table 2.1: Computation time for continuum model and hybrid model with different number of leukocytes and bacteria with same population each. Twenty realization is conducted to have mean CPU time and variance.

	Mean CPU time(s)	Variance
Continuum Model	6.4597132	0.050070843766150
10 particles	0.2808018	0.001460178720060
100 particles	1.0296066	0.015672598656790
250 particles	3.3602622	0.016801690465362
500 particles	5.7595568	0.016198336129357
1000 particles	14.052570	0.040144665600025
5000 particles	25.263758	1.430611099335806

We impose boundary conditions and initial condition assuming that the skin surface locates at $x = x_s$ and that the capillary transporting blood or the venule is found at distance $x = x_f$ from the skin surface. There is not chemo-attractant at $t = t_0$, though bacteria and leukocyte locates very close to the skin surface and the

blood vessel respectively.

$$\mathcal{A}(x, t_0) = 0, \tag{2.28}$$

$$\mathcal{B}(x, t_0) = f_x, \quad f_x = \mathcal{B}_0 \delta(x - (x_s + \epsilon)), \tag{2.29}$$

$$\mathcal{C}(x, t_0) = g_x, \quad g_x = \mathcal{C}_0 \delta(x - (x_f - \epsilon)), \tag{2.30}$$

where ϵ is very small value, $0 < \epsilon \ll 1$. We assume that bacteria remain on the finite domain with very small motility compared with that of leukocytes'($\mu_b \ll \mu$). This leads us to assume that chemo-attractants have the constant concentration at $x = x_s$ though they diffuse into the vessel at $x = x_f$.

$$\frac{\partial \mathcal{B}(x_s, t)}{\partial x} = 0, \quad \frac{\partial \mathcal{B}(x_f, t)}{\partial x} = 0, \tag{2.31}$$

$$\frac{\partial \mathcal{C}(x_s, t)}{\partial x} = 0, \quad \frac{\partial \mathcal{C}(x_f, t)}{\partial x} = 0, \tag{2.32}$$

$$\mathcal{A}(x_s, t) = \mathcal{A}_0, \quad \frac{\partial \mathcal{A}(x_f, t)}{\partial x} = h_a \mathcal{A}(x_f, t), \tag{2.33}$$

Eq.(2.31) and Eq.(2.32) imply that bacteria and leukocytes neither enter nor leave a domain of $x \in (x_s,\ x_f)$ and these boundary conditions are translated into reflective boundaries explained in section 2.1.1. Initial number of bacteria molecules and leukocytes molecules are $\mathcal{B}_0 = 8000$, and $\mathcal{C}_0 = 8000$. And initial concentration of chemo-attractans is $\mathcal{A}_0 = 10^{-5} M$ at $x = x_s$. The results of hybrid method is compared with continuum method solved by finite volume method(FVM) using operator-splitting method such as chemotaxis-motility step and reaction step. Total value diminishing

method is used for chemotaxis(advection) and implicit method for motility(diffusion). And Newton-raphson method is used to solve (stiff) reaction step.

In both method, concentration and existing number of the bacteria and the leukocytes are normalized with initial concentration and initial number of input cells. The comparison result is shown in Fig. 2.4. Leukoyctes move randomly due to random motility μ and toward the location of higher concentration of chemo-attractant with chemotaxis process. Bacteria and leukocytes meet around 1.5×10^{-4} from the wound site and are removed. Here our hybrid model shows exactly same as deterministic model with oscillation owing to stochastic effect. The random motility of bacteria, μ_b, is set as 10^{-12} to see the location of reaction occurrence clearly where leukocytes meet bacteria.

In one dimensional model, we measure the calculation time until $3000s$ using Intel(R) Core(TM) i7-2600 CPU @ 3.40GHz. Mean CPU time and variance are calculated from twenty realizations. Calculation time of continuum scale and different initial number of particles are reported in Table 2.2.2. In continuum model, space is discretized with two hundred elements(cells) and time step is set as $\min\{\Delta x^2/2D,\ \Delta x/|\mathbf{v}|\}$ considering Pèclet number. Hybrid method is valuable under small number of particles and our method is much faster in the view of computational time.

Table 2.2: Parameters for diffusion, reaction and chemotaxis

Notation	Description	Value[Unit]
D	diffusion coefficient of chemo-attractant	10^{-8} $[m^2 \cdot s^{-1}]$
μ_b	random motility of bacteria	10^{-15} $[m^2 \cdot s^{-1}]$
μ	random motility of leukocyte	calculated in Eq.(2.7)
kp	production rate of bacteria	10^{-6} $[s^{-1}]$
kg	generation rate of bacteria	3.47×10^{-5} $[s^{-1}]$
$k_d (= g_1)$	decay rate of bacteria/leukocyte	calculated in Eq.(2.4)
g_0	decay rate of leukocyte	1.65×10^{-6} $[s^{-1}]$
Avo	Avogadro's number	$6.022140857 \times 10^{23}$ $[mol^{-1}]$
r_b	radius of bacteria	$0.8 - 1.2$ $[\mu m]$
r_c	radius of leukocyte	$8 - 20$ $[\mu m]$
T_p	persistant time	300 $[s]$
v	chemotactic velocity	1.2 $[\mu m \cdot s^{-1}]$
χ_0	chemotactic sensitivity	4.0×10^{-8} $[s^{-1}]$
N_T	total number of cell receptors on the cell membrane	5.0×10^{10} $[\cdot]$
K_d	receptor dissociation constant	2.0×10^{-8} $[s^{-1}]$

2.2.3 Hybrid method results in two dimensional behavior

Concentrations of chemo-attractants($\mathcal{A}$), bacteria($\mathcal{B}$) and leukocytes($\mathcal{C}$) are delineated by chemotaxis-motility-reaction equations in the similar method of one dimensional model with two spatial dimensional domain, $\Omega \in [x_s\,, x_f] \times [y_s\,, y_f]$ and temporal dimension, $t \in [t_0\,, t_f]$.

$$\frac{\partial \mathcal{A}(\mathbf{x}, t)}{\partial t} = D\nabla^2 \mathcal{A}(\mathbf{x}, t) + k_p \mathcal{B}(\mathbf{x}, t) \tag{2.34}$$

$$\frac{\partial \mathcal{B}(\mathbf{x}, t)}{\partial t} = \mu_b \nabla^2 \mathcal{B}(\mathbf{x}, t) + (k_g - k_d \mathcal{C}(\mathbf{x}, t))\mathcal{B}(\mathbf{x}, t) \tag{2.35}$$

$$\frac{\partial \mathcal{C}(\mathbf{x}, t)}{\partial t} = -\nabla \cdot \mathbf{J_c}(\mathbf{x}, t) - (g_0 - g_1 \mathcal{B}(\mathbf{x}, t))\mathcal{C}(\mathbf{x}, t), \tag{2.36a}$$

$$\mathbf{J_c} = -\mu\nabla\mathcal{C}(\mathbf{x},t) + \mathcal{C}(\mathbf{x},t)\mathbf{V_c}(\mathcal{A},\Delta\mathcal{A}), \tag{2.36b}$$

$$\mathbf{V_c}(\mathcal{A},\Delta\mathcal{A}) = (\mathbf{v}\cdot\boldsymbol{\phi})\mathbf{e} = v_i\frac{\chi_0\frac{K_d+\mathcal{A}}{(K_d+\mathcal{A})^2}\frac{\partial\mathcal{A}}{\partial x_i}}{1+\chi_0\frac{K_d+\mathcal{A}}{(K_d+\mathcal{A})^2}\frac{\partial\mathcal{A}}{\partial x_i}}e_i \tag{2.36c}$$

where $\mathbf{V_c}$ is the chemotaxis velocity and is computed in each coordinate. v_i and $\boldsymbol{\phi}$ is the maximum velocity and the oriental bias in each direction of coordinate respectively. The initial condition of bacteria is that all bacteria cells($\mathcal{B}_0$) locate at the same position nearby the skin surface and that of leukocytes is that there are three different locations with the number of them($\mathcal{C}_{01}$,$\mathcal{C}_{02}$, and $\mathcal{C}_{03}$) underneath the blood vessel. The distance of initial locations are assumed that they are two or three endothelial cells apart.

$$\mathcal{A}(x,y,t_0) = 0, \tag{2.37}$$

$$\begin{aligned}\mathcal{B}(x,y,t_0) &= f(x,y),\\ f(x,y) &= \mathcal{B}_0\delta(x-x_{B0})\delta(y-y_{B0}),\end{aligned} \tag{2.38}$$

$$\begin{aligned}\mathcal{C}(x,y,t_0) &= g(x,y),\\ g(x,y) &= \sum_i \mathcal{C}_{0i}\delta(x-x_{Ci})\delta(y-y_{Ci}),\end{aligned} \tag{2.39}$$

where the initial position of bacteria (x_{B0}, y_{B0}) is ($0.5L_x$, $y_s+\epsilon$) and the initial positions of leukocyte, (x_{C1}, y_{C1}), (x_{C2}, y_{C2}) and (x_{C3}, y_{C3}) are ($0.3L_x$, $y_f-\epsilon$), ($0.5L_x$, $y_f-\epsilon$), and ($0.7L_x$, $y_f-\epsilon$) respectively. ϵ is very small value, $0<\epsilon\ll 1$ and L_x is the length of domain, $L_x = x_f - x_s$. We assume that bacteria remains on the finite domain with

very small motility compared with that of leukocyte's($\mu_b \ll \mu$) same as one dimensional model. We impose the dirichlet boundary condition of chemo-attractant at ($0.5L_x$, y_s) though it diffuses into the vessel at $y = y_s$. Leukocyte is assumed to have no flux boundary.

$$\begin{aligned}
&\frac{\partial \mathcal{A}(x_s, y, t)}{\partial x} = 0, \frac{\partial \mathcal{A}(x_f, y, t)}{\partial x} = 0, \frac{\partial \mathcal{A}(x_1, y_s, t)}{\partial y} = 0, \\
&\frac{\partial \mathcal{A}(x, y_f, t)}{\partial x} = h_a A(x, y_f, t), \quad \mathcal{A}(0.5L_x, y_s, t) = \mathcal{A}_0
\end{aligned} \tag{2.40}$$

$$\begin{aligned}
&\frac{\partial \mathcal{B}(x_s, y, t)}{\partial x} = 0, \quad \frac{\partial \mathcal{B}(x_f, y, t)}{\partial x} = 0, \\
&\frac{\partial \mathcal{B}(x, y_s, t)}{\partial y} = 0, \quad \frac{\partial \mathcal{B}(x, y_f, t)}{\partial x} = 0,
\end{aligned} \tag{2.41}$$

$$\begin{aligned}
&\frac{\partial \mathcal{C}(x_s, y, t)}{\partial x} = 0, \quad \frac{\partial \mathcal{C}(x_f, y, t)}{\partial x} = 0, \\
&\frac{\partial \mathcal{C}(x, y_s, t)}{\partial y} = 0, \quad \frac{\partial \mathcal{C}(x, y_f, t)}{\partial x} = 0,
\end{aligned} \tag{2.42}$$

where x_1 is $x_1 \in [x_s, 0.5L_x) \cup (0.5L_x, x_f]$. Concentration profile of chemo-attratants is solved by mesh-based continuum model using Finite Volume Method(FVM). Bacteria randomly work with the random motility(μ_b) and leukocyte drift with the random motility and the chemotactic velocity ($\mathbf{V_c}$) which is computed from the concentration of chemo-attractants and the concentration gradient of it considering the location of each leukocyte. And they undergo the reflective boundary condition and the initial condition with certain number of them(N_0^B, N_0^C, N_1^C, N_2^C). We use Gillespie Multi-Partilce method solving reaction within the range of properly assigned region.

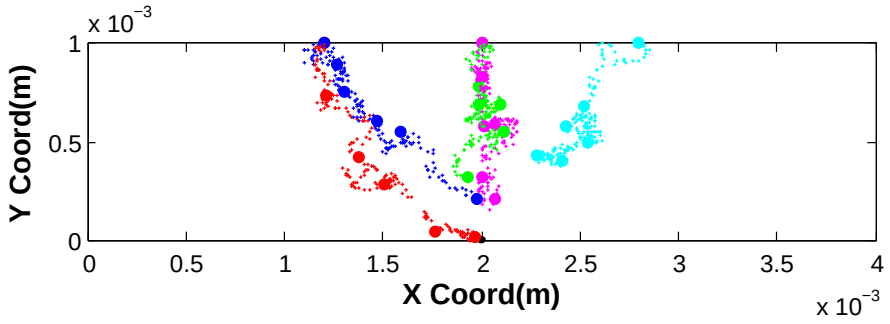

(a) Bacteria and Leukocyte

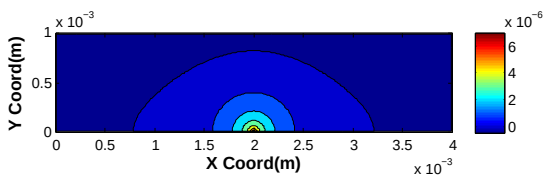

(b) Chemo-attractant

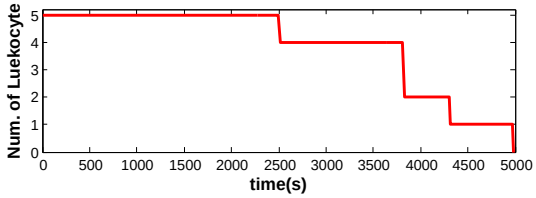

(c) Number of Leukocyte as time

Figure 2.5: Results in 2D simulation; (a) Traces of five different particles. Thicker dots show at the time of $0.0s$, $505.04s$, $1010.1s$, $1010.1s$, $1501.5s$, $2006.5s$, $2497.9s$. (b) Distribution of chemo-attractant at $1010.1s$. (c) Number of leukocyte with respect to time.

The behavior of leukocytes chemotaxis-motility-reaction with bacteria under two dimensional hybrid method is formulated in Eq.(2.34)–Eq.(2.36c). Its initial condition is Eq.(2.37)–Eq.(2.39) and boundary condition is Eq.(2.40)–Eq.(2.42) under spatial domain, $\Omega \in [x_s,\, x_f] \times [y_s,\, y_f]$ and temporal dimension, $t \in [t_0,\, t_f]$. And we impose the domain as $[x_s,\, x_f] = [0,\, 4 \times 10^{-4}m]$, $[y_s,\, y_f] = [0,\, 10^{-4}m]$ and the dirichlet boundary condition of chemo-attractants as $\mathcal{A}_0 = 10^{-5}M$. The profile of chemo-attractants is solved in continuum scale with Eq.(2.15b). Chemo-attractants diffuse into cells and leak out with the slope of h_a at $y = y_f$ where capillary vessel locates. Bacteria move into cell with much smaller random motility(μ_b) than that of leukocyte's(μ). Bacteria move little in our time scale while leukocytes transfer from the capillary vessel to the wound site. Bacteria could be reproduced with the rate of k_g and removed by leukocyte's metabolism. Leukocytes attach and roll over the vessel wall. And they transmigrate through endothelial cells of the capillary vessel and chemotaxis to the wound site during the inflammation process. We focus the process after transmigration of leukocytes. Leukocytes initially locate at the $y = y_f$ considered as the capillary location, and different positions in x-direction.

Results of two dimensional hybrid method are shown in Fig. 2.5. Lekocytes move to the wound site with different path ways though they start at the same position due to its random motion. But all the particles move toward to the source of chemo-attractants with chemotaxis motion. Five different colors represent the traces

of different particles and bigger solid dots are at the position at the certain time step. When a leukocyte coincides with a bacteria, both undergo reaction with GMP method. We control the time step considering Pe and Da with shown algorithm in section 2.1.4. This result shows that the movement of any leukocyte inside the domain with any initial position follows the chemotactic behavior with respect to the distribution of chemo-attractants and the gradient of it. And they have good agreement of reaction process with GMP method. The novel hybrid algorithm of ours could perfectly describe the process of the lekocyte's behavior of small concentration.

2.3 SUMMARY and CONCLUSION

Chemo-attractants mainly diffuse into skin or wounded cell from wound site where bacteria invade. And leukocytes detect the gradient of chemo-attractant's concentration and move to higher concentration where bacteria to be located. The motility of bacteria is much smaller than that of leukocyte's, and this smaller motility causes bacteria to move little within same time scale of leukocyte's movement. Leukocytes decrease due to dying during inflammation process not only because of natural dying, but also phagocytosis action by moving to the wound site and engulfing and degrading bacteria. Here we assumes one leukocyte could kill only one bacteria. Bacteria decrease after leukocyte's phagocytosis action but increase because of duplication as

well. These process need multi-scale algorithm due to its wide range of time scale and length scale.

Wide range of spatial or temporal simulation in complex biological problem cause a big burden of computational capacity and time when we use continuum scale modeling about an accuracy, especially handling small concentration problems. We develop hybrid algorithm implementing continuum and stochastic method for chemotaxis-motility-reaction problem. Leukocytes and bacteria move randomly and the quantity of random motion is solved using Brownian motion. Chemotaxis is a form of advection and it is expressed as particle tracking dependent on the concentration and the concentration gradient of chemo-attractant which are solved in continuum scale. Reaction is solved by using modified Gillespie multi-particle method considering the chemical master equation. We consider the cell Pèclet number to determine diffusion- or advection-dominated scheme. Every particle could have different velocity and it is possible to have shorter time than diffusion time step and we need to choose shorter time step to decide reasonably after making comparison with reaction time step. And Damköhler number to take account for the time scale between transferring phenomenon(random motility and chemotaxis) and multi-particle reaction. Our algorithm produces good result when we use many particles compared with continuum model but takes longer. But we focus small number or small concentration and it is much faster than continuum model and show the stochastic character of it. We suggest more realistic and solid

model in chemotaxis-motility-reaction by hybrid model.

Um, K. and D. M. Tartakovsky, "Hybrid models of chemotaxis with application to leukocyte migration", in preparation

Chapter 3

Global sensitivity analysis in multi-scale problem with independent input variables

Pore- and Darcy-scale models provide two distinct descriptors of flow and transport in porous media. The former approach relies on relatively few modeling assumptions but requires the detailed knowledge of a material's pore structure and is computationally prohibitive unless the number of pores being simulated is small. The latter approach invokes the concept of a representative elementary volume, treating a porous medium as an effective continuum without distinguishing the pore space and surrounding solid matrix. While orders of magnitude faster to solve than their

pore-scale counterparts, Darcy-scale models are grounded in a number of simplifying assumptions whose validity is often questionable [23, 24].

Upscaling techniques, such as homogenization via multiple-scale expansions [25] or the method of volume averaging [26], allow one to ascertain the applicability of Darcy-scale models both by identifying the necessary and sufficient conditions under which their foundational assumptions hold and by relating parameters in these models to pore geometry and operating regime. While many of these approaches formally place restrictions on the regularity of a pore structure (e.g., by requiring it to be periodic), they often yield remarkably robust predictions of macroscopic properties of materials with irregular pore structures with equivalent microscopic characteristics (e.g., porosity, pore-size distribution, connectivity) [25]. Recent examples of such studies include [27, 28, 29, 30], among many others. By mapping microscopic material properties onto their macroscopic counterparts, upscaling approaches of this kind instill confidence in predictions of transport processes in natural (e.g., geologic) porous media [31, 32] and facilitate design of new metamaterials [33, 34]. For example, since porous electrodes with high surface area have high energy density and, hence, high electrical double-layer capacitance (EDLC) [35], much of recent effort focused on synthesis of nanostructured electrodes with high surface area [36]. However, as a specific surface area of nanoporous materials continues to increase, their EDLC cannot be generated at high power density if ions in the electrolyte cannot diffuse fast enough. Attempts to increase ion diffusion

by altering electrolyte molecules or salts were shown to adversely change the intrinsic chemical stability [37]. Instead, an observation that ordered nanopores increase ion diffusion [38] suggests a multi-objective optimization problem, in which specific surface area and diffusion coefficients are two quantities of interest.

One of the least studied aspects of multiscale simulations of transport phenomena in porous media is sensitivity of their results to changes in pore geometry. Yet, high sensitivity would undermine the generality of a detailed pore-scale investigation, based on either computer-generated or imaged pore spaces of a porous material. Likewise, a metamaterial's design that is excessively sensitive to parameters controlling its pore structure is unlikely to be of much practical use. Homogenization-based relationships between pore-scale parameters and their Darcy-scale counterparts facilitate both sensitivity analysis (SA) and uncertainty quantification (UQ) in this multiscale setting.

A prevalent UQ framework treats uncertain input parameters as random variables. Within this paradigm, sensitivity of a model's prediction to input parameters can be quantified in terms of relative contributions of variances of the input parameters to the prediction's variance. Such an approach to SA is often referred as analysis of variance or ANOVA; it is global in the sense that, unlike its local counterparts, it does not require identification of a base set of parameter values which is then sequentially perturbed on at a time. ANOVA is well suited for homogenization-based multiscale modeling since a base set of parameter values either is unknown/unknowable due to

pore-scale heterogeneity of natural (e.g., geologic) materials or has to be identified by solving a shape optimization problem (in the case of material design).

We develop these ideas in the context of multiscale modeling of reactive solutes diffusing through a (nano)porous material, while sorbing to its solid matrix. Pore- and Darcy-scale formulations of this problem are provided in Section 3.1. A global SA (GSA) of two macroscopic material properties, effective diffusion coefficient and effective sorption rate, to microscopic pore-geometric parameters is described in Section 3.2. In Section 3.3 we provide simulation results and discuss their implications for material design. Main conclusions derived from our study are summarized in Section 3.4.

3.1 Problem Formulation

Consider a volume $\mathcal{V} = \mathcal{P} \cup \mathcal{S}$ of a porous material, which comprises the fluid-filled pore space $\mathcal{P}$ and the solid matrix $\mathcal{S}$; the (multi-connected) fluid-solid interface is denoted by $\Gamma = \mathcal{P} \cap \mathcal{S}$. Following the standard practice in homogenization theory, we assume that the volume $\mathcal{V}$ consists of a periodic arrangement of unit cells $\mathcal{U} = \mathcal{P}_\mathcal{U} \cup \mathcal{S}_\mathcal{U}$ with the pore space $\mathcal{P}_\mathcal{U}$, solid matrix $\mathcal{S}_\mathcal{U}$, and the interface $\Gamma_\mathcal{U}$. Figure 3.1 provides a typical example of hierarchical nanoporous materials that exhibit such a structure.

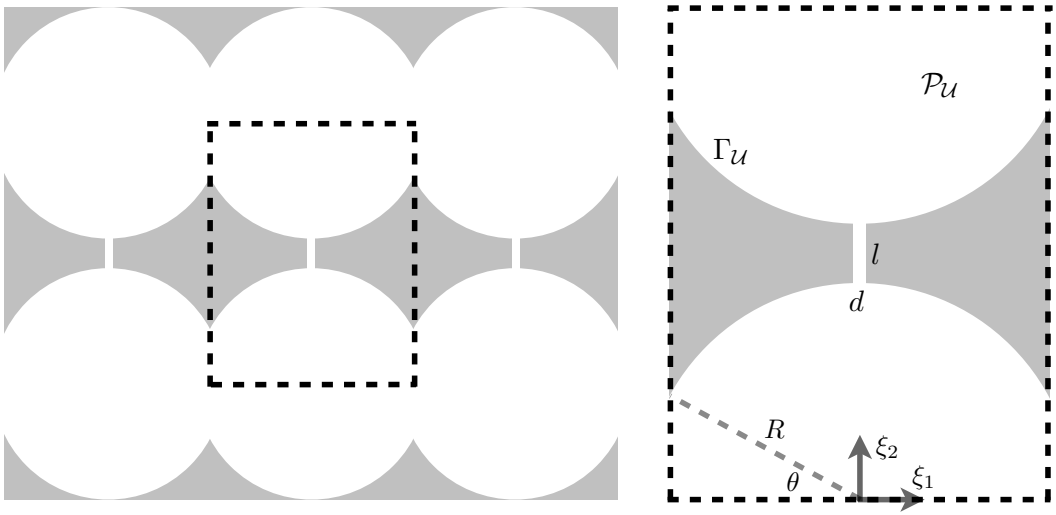

Figure 3.1: Schematic representation of a hierarchical nanoporous material (left) and its unit cell (right).

3.1.1 Pore-scale model

Let $c(\mathbf{x}, t)$ [mol/L^3] denote the solute concentration at a point $\mathbf{x} \in \mathcal{P}$ and time t. Its evolution within the pore space $\mathcal{P}$ is governed by a diffusion equation

$$\frac{\partial c}{\partial t} = \nabla \cdot (D \nabla c), \qquad \mathbf{x} \in \mathcal{P}, \quad t > 0, \tag{3.1}$$

where the spatial variability of the diffusion coefficient $D(\mathbf{x})$ [L^2/T] accounts for the possibility of having Fickian diffusion in mesopores and Knudsen diffusion in nanotubes (see Fig. 3.1). Equation (3.1) is subject to a uniform initial condition

$$c(\mathbf{x}, 0) = c_{\text{in}}, \qquad \mathbf{x} \in \mathcal{P}. \tag{3.2}$$

A boundary condition at the fluid-solid interface Γ with unit normal vector $\mathbf{n}(\mathbf{x})$ is constructed from mass conservation, such that the normal component of the solute

mass flux, $-D\mathbf{n}\cdot\nabla c$, is balanced by the rate change of absorbed solute,

$$-D\mathbf{n}\cdot\nabla c = q_{\mathrm{m}}\frac{\partial s}{\partial t}, \qquad \mathbf{x}\in\Gamma, \quad t>0, \tag{3.3a}$$

where $q(\mathbf{x},t) = q_{\mathrm{m}}s(\mathbf{x},t)$ is the adsorption amount per unit area of the Γ [mol/L^2], q_{m} [mol/L^2] is the maximal adsorption amount, and $s(\mathbf{x},t)$ is the fractional coverage of Γ. The latter is assumed to follow Lagergren's pseudo-first-order rate equation [39, 40],

$$\frac{\mathrm{d}s}{\mathrm{d}t} = \gamma(s_{\mathrm{eq}} - s), \tag{3.3b}$$

where γ [1/T] is the adsorption rate constant and the equilibrium adsorption coverage fraction s_{eq} satisfies Langmuir's adsorption isotherm

$$s_{\mathrm{eq}} = \frac{Kc}{1+Kc} \tag{3.3c}$$

with the adsorption equilibrium constant K [L^3/mol].

3.1.2 Darcy-scale model

Darcy-scale models treat a porous material as a continuum, without separating fluid and solid phases. Thus, a volume-averaged concentration,

$$C(\mathbf{x},t) \equiv \frac{1}{\|\mathcal{U}\|}\int\limits_{\mathcal{U}(\mathbf{x})} c(\boldsymbol{\xi},t)\mathrm{d}\boldsymbol{\xi} = \frac{1}{\|\mathcal{U}\|}\int\limits_{\mathcal{P}_{\mathcal{U}}(\mathbf{x})} c(\boldsymbol{\xi},t)\mathrm{d}\boldsymbol{\xi} = \frac{\phi}{\|\mathcal{P}_{\mathcal{U}}\|}\int\limits_{\mathcal{P}_{\mathcal{U}}(\mathbf{x})} c(\boldsymbol{\xi},t)\mathrm{d}\boldsymbol{\xi}, \qquad \mathbf{x}\in\mathcal{V}, \tag{3.4}$$

is defined at every "point" $\mathbf{x}$ of the material $\mathcal{V}$. Here, $\|\cdot\|$ indicates the volume of the corresponding domain, and $\phi \equiv \|\mathcal{P}_{\mathcal{V}}\|/\|\mathcal{V}\| = \|\mathcal{P}_{\mathcal{U}}\|/\|\mathcal{U}\|$ is the porosity. Generalizing the homogenization via multiple-scale expansions in [33] to account for spatial

variability of D, it is easy to show that the Darcy-scale solute concentration $C(\mathbf{x}, t)$ satisfies a reaction-diffusion equation

$$\phi \frac{\partial C}{\partial t} = \nabla \cdot (\mathbf{D}_{\text{eff}} \nabla C) - \phi q_{\text{m}} \gamma_{\text{eff}} \frac{KC}{1 + KC}, \tag{3.5}$$

where "the effective rate constant" γ_{eff} [1/L] is defined in purely geometric terms,

$$\gamma_{\text{eff}} = \frac{||\Gamma_{\mathcal{U}}||}{||\mathcal{P}_{\mathcal{U}}||}, \tag{3.6}$$

while the effective diffusion coefficient $\mathbf{D}_{\text{eff}}$, a second-rank tensor, depends on both pore geometry and pore-scale processes. Specifically, it is computed as

$$\mathbf{D}_{\text{eff}} = \frac{1}{||\mathcal{U}||} \int_{\mathcal{P}_{\mathcal{U}}} (\mathbf{I} + \nabla_{\boldsymbol{\xi}} \boldsymbol{\chi}^{\top}) \mathrm{d}\boldsymbol{\xi}, \tag{3.7a}$$

where $\mathbf{I}$ is the identity matrix and the closure variable $\boldsymbol{\chi}(\boldsymbol{\xi})$, a $\mathcal{U}$-periodic vector defined on $\mathcal{P}_{\mathcal{U}}$, satisfies a Laplace equation

$$\nabla_{\boldsymbol{\xi}} \cdot (D \nabla_{\boldsymbol{\xi}} \boldsymbol{\chi}) = \mathbf{0}, \qquad \boldsymbol{\xi} \in \mathcal{P}_{\mathcal{U}} \tag{3.7b}$$

and the normalizing condition

$$\langle \boldsymbol{\chi} \rangle \equiv \frac{1}{||\mathcal{U}||} \int_{\mathcal{P}_{\mathcal{U}}} \boldsymbol{\chi}(\boldsymbol{\xi}) \mathrm{d}\boldsymbol{\xi} = \mathbf{0}. \tag{3.7c}$$

Equation (3.7b) is subject to the boundary condition along the fluid-solid segments $\Gamma_{\mathcal{U}}$,

$$\mathbf{n} \cdot \nabla_{\boldsymbol{\xi}} \boldsymbol{\chi} = -\mathbf{n} \cdot \mathbf{I}, \qquad \boldsymbol{\xi} \in \Gamma_{\mathcal{U}}; \tag{3.7d}$$

and the $\mathcal{U}$-periodic boundary conditions along the remaining ("fluid") segments Γ_f of the boundary of $\mathcal{P}_\mathcal{U}$. In the case of the hierarchical nanoporous material shown in Figure 3.1, these take the form

$$\chi_1(-a, \xi_2) = \chi_1(a, \xi_2) = 0, \qquad \frac{\partial \chi_1}{\partial \xi_2}(\xi_1, 0) = \frac{\partial \chi_1}{\partial \xi_2}(\xi_1, b) = 0, \tag{3.7e}$$

and

$$\chi_2(\xi_1, 0) = \chi_2(y_1, b) = 0, \qquad \frac{\partial \chi_2}{\partial \xi_1}(-a, \xi_2) = \frac{\partial \chi_2}{\partial \xi_1}(a, \xi_2) = 0, \tag{3.7f}$$

where $a = R\cos\theta$ and $b = 2R + l$. Here, R is the mesopore radius; θ is the angle of overlap between any two adjacent mesopores in a nano-tunnel; and d and l are, respectively, the diameter and length of nanotubes which serve as nano-bridges between adjacent nano-tunnels.

3.2 Global Sensitivity Analysis and Uncertainty Quantification

Equations (3.6) and (3.7) map the pore-structure parameters $\mathbf{p} = \{R, \theta, d, l\} \equiv \{p_1, \cdots, p_4\}$ onto the macroscopic material properties,

$$\mathbf{D}_{\text{eff}} = \mathbf{D}_{\text{eff}}(\mathbf{p}), \qquad \gamma_{\text{eff}} = \gamma_{\text{eff}}(\mathbf{p}). \tag{3.8}$$

These maps allow us both to investigate sensitivity of the macroscopic parameters to variations in the pore geometry and to relate uncertainty in the latter to uncertainty

in the former. We treat the uncertain parameters p_i $(i = 1, \cdots, 4)$ as statistically independent random variables with probability density functions (PDFs) f_{p_i}, so that the joint PDF of $\mathbf{p}$ is $f_{\mathbf{p}} = \prod f_{p_i}$. This simplifying assumption is made to facilitate the subsequent variance-based sensitivity analysis, even though the geometrical properties characterizing a pore structure are generally interdependent.

We present our global sensitivity analysis (GSA) and uncertainty quantification (UQ) for the longitudinal diffusion coefficient $D_{\text{eff}}^{11} \equiv D_{\text{L}}(\mathbf{p})$. All the other functions of $\mathbf{p}$ in (3.8) are treated identically.

3.2.1 Global Sensitivity Analysis

Thorough expositions of the GSA can be found in several monographs [41, 42], here we briefly describe it in terms relevant to our study. The (explicitly unknown) function $D_{\text{L}}(\mathbf{p})$ has a unique expansion into summands of $\mathbf{p} = \{p_1, \cdots, p_4\}$, e.g. [43],

$$D_{\text{L}}(\mathbf{p}) = D_0 + \sum_{i=1}^{4} D_i(p_i) + \sum_{i=1}^{4} \sum_{j<i} D_{ij}(p_i, p_j) + \cdots + D_{1234}(p_1, \cdots, p_4), \tag{3.9a}$$

where

$$D_0 = \int_{\mathbb{R}^4} D_{\text{L}} \mathrm{d}\mathbf{p}; \qquad D_i = \int_{\mathbb{R}^3} D_{\text{L}} \prod_{k \neq i} \mathrm{d}p_k - D_0, \quad i \geq 1; \tag{3.9b}$$

$$D_{ij} = \int_{\mathbb{R}^2} D_{\text{L}} \prod_{k \neq i,j} \mathrm{d}p_k - D_0 - D_i - D_j, \tag{3.9c}$$

etc. By construction, for all summands,

$$\int_{\mathbb{R}} D_{i_1\cdots i_s}\mathrm{d}p_{i_k} = 0 \quad \text{and} \quad \int_{\mathbb{R}^4} D_{i_1\cdots i_s}D_{j_1\cdots j_r}\mathrm{d}\mathbf{p} = 0. \tag{3.10}$$

The ensemble mean and variances of $D_{\mathrm{L}}(\mathbf{p})$ are defined as

$$\langle D_{\mathrm{L}}\rangle = \int_{\mathbb{R}^4} D_{\mathrm{L}}(\mathbf{p}')f_{\mathbf{p}}(\mathbf{p}')\mathrm{d}\mathbf{p}' \quad \text{and} \quad \sigma^2_{D_{\mathrm{L}}} = \int_{\mathbb{R}^4} D^2_{\mathrm{L}}(\mathbf{p}')f_{\mathbf{p}}(\mathbf{p}')\mathrm{d}\mathbf{p}' - \langle D_{\mathrm{L}}\rangle^2, \tag{3.11}$$

respectively. Substituting (3.9) into (3.11), while accounting for the orthogonality condition (3.10), yields the so-called analysis of variance (ANOVA) decomposition,

$$\sigma^2_{D_{\mathrm{L}}} = \sum_{i=1}^{N_{\mathrm{par}}}\sigma_i^2 + \sum_{i=1}^{N_{\mathrm{par}}}\sum_{j<i}\sigma_{ij}^2 + \cdots + \sigma^2_{1234}, \tag{3.12}$$

where the partial variances $\sigma^2_{i_1\cdots i_s}$ are computed as

$$\sigma^2_{i_1\cdots i_s} = \int_{\mathbb{R}^4} D^2_{i_1\cdots i_s}(p'_{i_1}\cdots p'_{i_s})f_{\mathbf{p}}(\mathbf{p}')\mathrm{d}\mathbf{p}'. \tag{3.13}$$

The Sobol' sensitivity indices [44] are defined by dividing both sides of (3.12) with $\sigma^2_{D_{\mathrm{L}}}$, such that the first- and second-order Sobol' indices are defined as

$$S_i = \frac{\sigma_i^2}{\sigma^2_{D_{\mathrm{L}}}} \quad \text{and} \quad S_{ij} = \frac{\sigma_{ij}^2}{\sigma^2_{D_{\mathrm{L}}}}, \tag{3.14}$$

respectively. The total Sobol' sensitivity index, which quantifies the total effect of uncertainty in the ith parameter p_i on the overall uncertainty in the macroscopic parameter D_{L}, is

$$T_i = \frac{1}{\sigma^2_{D_{\mathrm{L}}}}\sum_{\alpha\in I_i}\sigma_\alpha^2 \tag{3.15}$$

where I_i is the set of all subset of $\{p_1, \cdots, p_4\}$ containing the ith parameter.

The statistical moments in (3.11)–(3.15) can be estimated with, e.g., Monte Carlo simulations (MCS) consisting of N_{MCS} deterministic solves of (3.7) in which realizations $\tilde{\mathbf{p}}_i$ $(i = 1, \cdots, N_{\mathrm{MCS}})$ of the pore-scale parameters $\mathbf{p}$ are drawn from the distribution $f_{\mathbf{p}}$, such that

$$\tilde{\sigma}^2_{D_{\mathrm{L}}} = \frac{1}{N_{\mathrm{MCS}} - 1} \sum_{i=1}^{N_{\mathrm{MCS}}} D^2_{\mathrm{L}}(\tilde{\mathbf{p}}_i) - \langle \tilde{D}_{\mathrm{L}} \rangle, \qquad \langle \tilde{D}_{\mathrm{L}} \rangle = \frac{1}{N_{\mathrm{MCS}}} \sum_{i=1}^{N_{\mathrm{MCS}}} D_{\mathrm{L}}(\tilde{\mathbf{p}}_i). \tag{3.16}$$

This MCS procedure has a slow convergence rate of $\sim 1/\sqrt{N_{\mathrm{MCS}}}$. One alternative, which we pursue in this study, is to use the stochastic collocation method [45]. This approach to GSA is nonintrusive, in that it can be seamlessly combined with any solver used to solve deterministic realizations of (3.7), e.g., the finite element method in `COMSOL` used in our simulations. We deployed the GSA implementation in the software `DAKOTA` [46].

3.2.2 Uncertainty Quantification

Uncertainty in the pore-scale parameters $\mathbf{p}$ gives rise to uncertainty in the macroscopic parameters, e.g., D_{L}. The latter is expressed in terms of its PDF $f_{D_{\mathrm{L}}}(\eta)$, which is computed as follows. First, we deploy `DAKOTA` [46] to construct a surrogate model of $D_{\mathrm{L}}(\mathbf{p})$ by using a (generalized) polynomial chaos expansion (PCE) [47, 48, 49],

truncated after $N_{\rm PCE}$ terms,

$$D_{\rm L}(\mathbf{p}) = \sum_{i=0}^{\infty} \hat{D}_i \Psi_i(\mathbf{p}) \approx \sum_{i=0}^{N_{\rm PCE}-1} \hat{D}_i \Psi_i(\mathbf{p}), \qquad N_{\rm PCE} - 1 = \frac{(n+N_{\rm par})!}{n! N_{\rm par}!}, \tag{3.17}$$

where n is the polynomial degree, $\Psi_i(\mathbf{p})$ are the orthogonal multivariate polynomials and $\hat{D}_i$ are the expansion coefficients. The set of $\Psi_i(\mathbf{p})$ is derived from the Askey scheme of hypergeometric orthogonal polynomials [48] to match continuous PDFs of $N_{\rm par} = 4$ parameters $\mathbf{p}$, specifically, since in the simulations reported below each p_k ($k = 1, \cdots, 4$) follows a uniform distribution, $\Psi_i(\mathbf{p})$ are multivariate Legendre polynomials. Convergence properties of (3.17) have been the subject of many studies [48]. Figure 3.2 demonstrates the convergence of estimates of the ensemble means $\langle D_{\rm L} \rangle$, $\langle D_{\rm T} \rangle$, and $\langle \gamma_{\rm eff} \rangle$ in terms of both the polynomial degree n and the number of samples used to computed the means from (3.17). Based on these results, we use $n = 4$ ($N_{\rm PCE} = 626$) and $N_{D_{\rm L}} = N_{D_{\rm T}} = N_{\gamma_{\rm eff}} = 10^8$ samples in the simulation results presented below.

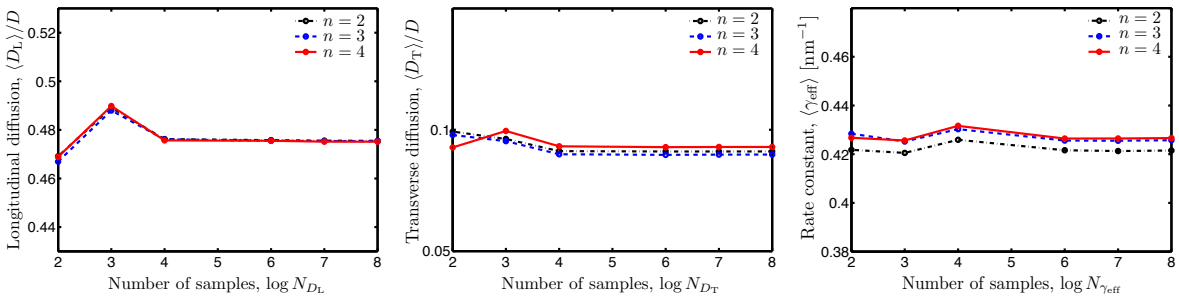

Figure 3.2: Ensemble means of the normalized longitudinal diffusion coefficient, $\langle D_{\rm L} \rangle / D$, normalized trnasverse diffusion coefficient, $\langle D_{\rm T} \rangle / D$ and rate constant, $\langle \gamma_{\rm eff} \rangle$. The means are computed from (3.17) with the second ($n = 2$), third ($n = 3$) and fourth ($n = 4$) degree polynomials, using respectively $N_{D_{\rm L}}$, $N_{D_{\rm T}}$ or $N_{\gamma_{\rm eff}}$ realizations of the mutually independent and uniformly distributed microscopic parameters $\mathbf{p} = \{R, \theta, d, l\}$.

Second, we use (3.17) to compute $N_{D_{\rm L}}$ samples of $D_{{\rm L}i} = D_{\rm L}(\tilde{\mathbf{p}}_i)$, with $i =$

$1, \cdots, N_{D_\mathrm{L}}$, corresponding to N_{D_L} realizations of the random parameter vector $\mathbf{p}$. Then, $f_{D_\mathrm{L}}(\eta)$ is computed with a kernel density estimator (KDE),

$$f_{D_\mathrm{L}}(\eta) = \frac{1}{N_{D_\mathrm{L}}\sqrt{2\pi h^2}} \sum_{i=1}^{N_{D_\mathrm{L}}} \exp\left[-\frac{(\eta - D_{\mathrm{L}i})^2}{2h^2}\right], \tag{3.18}$$

where h is the kernel bandwidth. Since uncertainty in the macroscopic parameters in (3.8) stems from their dependence on the same set of uncertain pore-scale parameters $\mathbf{p}$, they are expected to be correlated. Joint PDFs of the macroscopic parameters, e.g., the longitudinal (D_L) and transverse ($D^{22}_{\mathrm{eff}} \equiv D_\mathrm{T}$) components of the effective diffusion coefficient tensor $\mathbf{D}_{\mathrm{eff}}$, are estimated with a KDE as

$$f_{D_\mathrm{L}D_\mathrm{T}}(\eta_\mathrm{L}, \eta_\mathrm{T}) = \frac{1}{N_{D_\mathrm{L}} 2\pi h_\mathrm{L} h_\mathrm{T}} \sum_{i=1}^{N_{D_\mathrm{L}}} \exp\left[-\frac{(\eta_\mathrm{L} - D_{\mathrm{L}i})^2}{2h_\mathrm{L}^2} - \frac{(\eta_\mathrm{T} - D_{\mathrm{T}i})^2}{2h_\mathrm{T}^2}\right]. \tag{3.19}$$

Kernel bandwidths—h in (3.18), and h_L and h_T in (3.19)—are computed with the modified Sheather-Jones method [50].

Once computed, the (joint) PDFs of the macroscopic parameters $\mathbf{D}_{\mathrm{eff}}$ and γ_{eff} complete a probabilistic formulation of the Darcy-scale problem (3.5). This problem can be solved with any standard uncertainty quantification method, including the MCS and PCE described above.

3.3 Simulation Results

We consider the hierarchical nanoporous material, whose assembly template is shown in Figure 3.1. In the absence of information about the statistical properties

of the pore-scale parameters $\mathbf{p}$, we take each p_i $(i = 1, \ldots, 4)$ to have a uniform distribution on the respective interval $[p_i^{\min}, p_i^{\max}]$. (The methods described above can also accommodate more informative priors.) The values of $p_i^{\min}$ and $p_i^{\max}$, for $(i = 1, \ldots, 4)$, are reported in Table 3.1; the large intervals over which these parameters are allowed to vary are representative of typical variability of natural (e.g., geologic) materials or initial uncertainty about optimal values of pore-scale parameters used in material design. We used a constant value of molecular diffusion D throughout the pore space $\mathcal{P}_{\mathcal{U}}$.

Table 3.1: Intervals of determination, $[p_i^{\min}, p_i^{\max}]$, of the four pore-scale parameters describing the pore structure in Figure 3.1.

	$p_1 = R, [nm]$	$p_2 = \theta$, [rad]	$p_3 = d$, [nm]	$p_4 = l$, [nm]
$p_i^{\min}$	10.00	0.07	4.0	8.00
$p_i^{\max}$	60.00	0.70	8.0	18.00

For given values of the parameter set $\mathbf{p}$, i.e., for a given computational domain $\mathcal{P}_{\mathcal{U}}$ in Figure 3.1, first, the closure vector variable $\boldsymbol{\chi}(\boldsymbol{\xi})$ is computed by solving (3.7b)–(3.7f) with `COMSOL`. Second, the normalized components of the effective diffusion tensor, D_{L}/D and D_{T}/D, are computed by numerically evaluating the quadrature in (3.7a). The corresponding values of the effective rate constant γ_{eff} are computed with (3.6). The results of these calculations are exhibited in Figures 3.3 and 3.4. They demonstrate the complex interplay of the pore-scale parameters $\mathbf{p}$ and their opposing effects on the macroscopic material properties. While the effective diffusion coefficients D_{L}/D and

D_T/D increase with the mesopore radius R and overlap angle θ, the effective rate constant γ_{eff} decreases as these parameters increase.

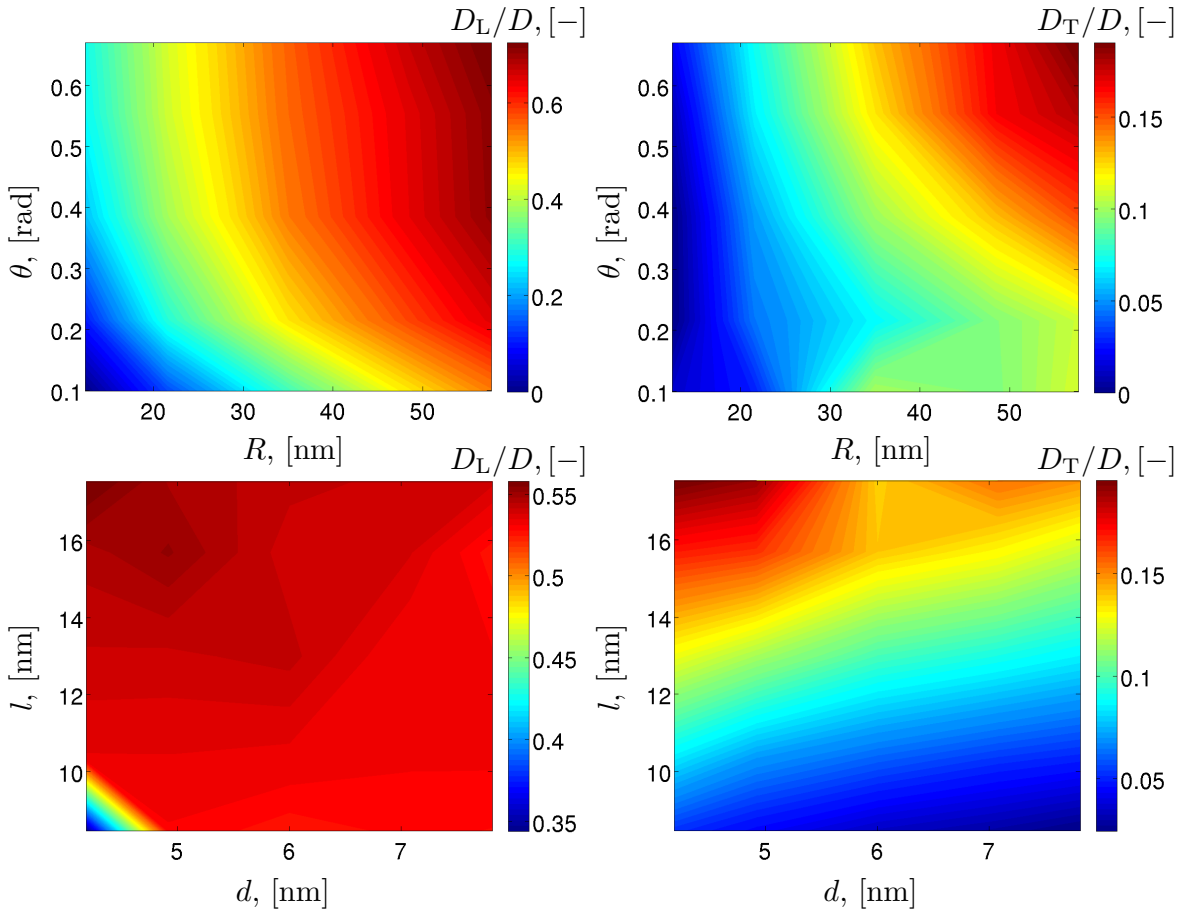

Figure 3.3: Dependence of the normalized longitudinal, D_L/D, (left column) and transverse, D_T/D, (right column) diffusion coefficients on R and θ for either fixed $l = 13.0$ nm and $d = 6.0$ nm (upper row) or d and l for fixed $R = 35.0$ nm and $\theta = 0.38$ (bottom row).

3.3.1 Global sensitivity analysis

Since the parameters $\mathbf{p}$ are uniformly distributed, we take $\Psi_i(\mathbf{p})$ in the PCE (3.17) to be Legendre polynomials; the series is truncated after $N_{PCE} - 1 = 625$ terms, i.e.,

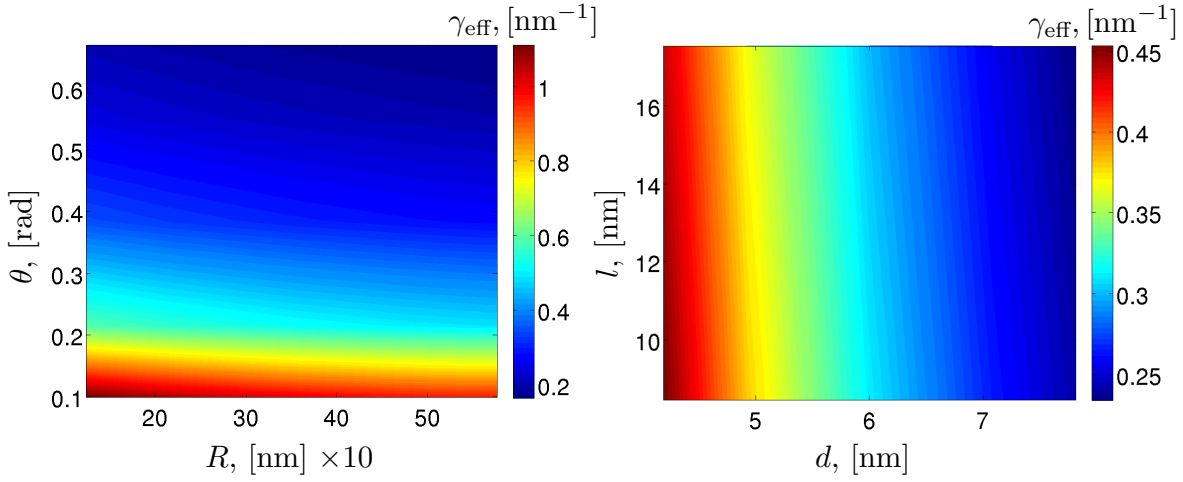

Figure 3.4: Dependence of the effective rate constant γ_{eff} [nm^{-1}] on R and θ for either fixed $l = 13.0$ nm and $d = 6.0$ nm (left) or d and l for fixed $R = 35.0$ nm and $\theta = 0.38$ (right).

using the $n = 4$ degree polynomials in the pore-scale parameter p_i $(i = 1, \ldots, 4)$, each of which is defined on its respective interval in Table 3.1. The longitudinal (D_{L}) and transverse (D_{T}) components of the effective diffusion coefficient $\mathbf{D}_{\text{eff}}$ and the effective reaction rate constant γ_{eff} are calculated for $N_{D_{\text{L}}} = N_{D_{\text{T}}} = N_{\gamma_{\text{eff}}} = 10^8$ realizations of the microscopic parameters $\{R, \theta, d, l\}$. These realizations are then used in (3.17) to compute the variances of the macroscopic parameters, and in (3.9)–(3.15) to compute the corresponding first-order and total Sobol' sensitivity indices. Table 3.2 summarizes the results of these calculations, and Figures 3.5 and 3.6 provide their visual representation.

Both the longitudinal (D_{L}) and transverse (D_{T}) components of the effective diffusion coefficient tensor $\mathbf{D}$ are most sensitive to the overlap angle θ, which determines the pore-throat size. While longitudinal diffusion coefficient D_{L} is virtually insensitive

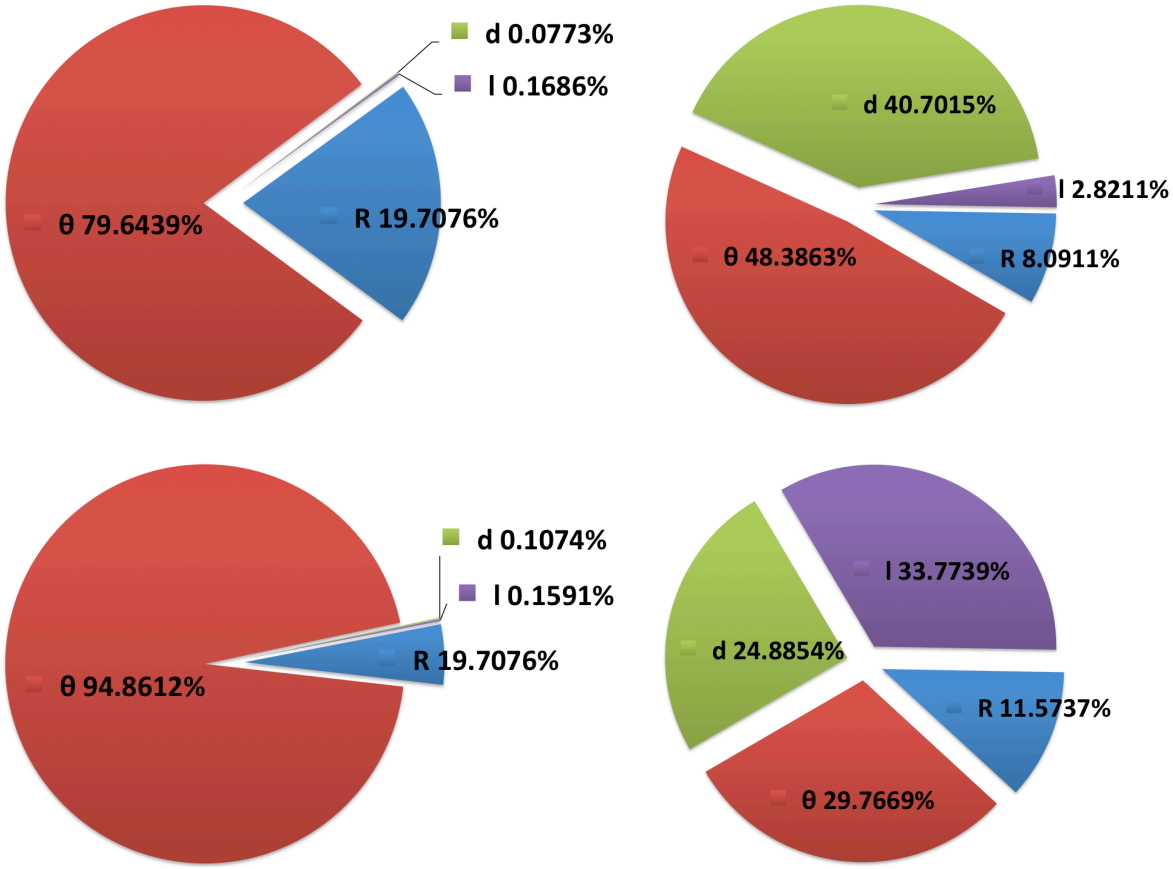

Figure 3.5: Relative contribution of the first-order (upper row) and total (bottom row) Sobol' sensitivity indices to the total variance of the longitudinal, D_{L}, (left column) and transverse, D_{T}, (right column) components of the effective diffusion tensor.

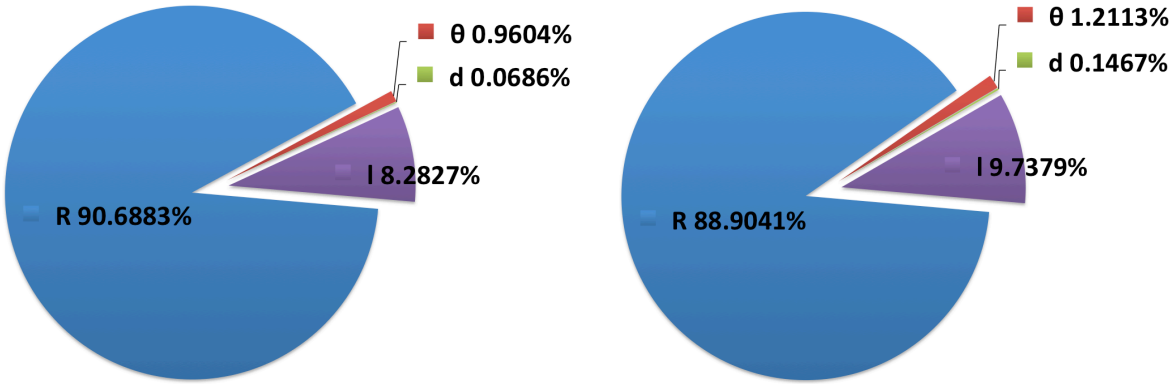

Figure 3.6: Relative contribution of the first-order (left) and total (right) Sobol' sensitivity indices to the total variance of γ_{eff}.

Table 3.2: The first-order (S) and total (T) Sobol' indices of effective longitudinal (D_{L}) and transverse (D_{T}) diffusion coefficients and effective rate constant (γ_{eff}) for the four pore-scale parameters $\mathbf{p} = \{R, \theta, d, l\}$.

	$S_{D_{\mathrm{L}}}$	$T_{D_{\mathrm{L}}}$	$S_{D_{\mathrm{T}}}$	$T_{D_{\mathrm{T}}}$	$S_{\gamma_{\mathrm{eff}}}$	$T_{\gamma_{\mathrm{eff}}}$
R	1.95×10^{-1}	4.90×10^{-2}	7.70×10^{-2}	1.92×10^{-1}	8.72×10^{-1}	9.09×10^{-1}
θ	7.73×10^{-1}	9.54×10^{-1}	4.61×10^{-1}	4.95×10^{-1}	9.29×10^{-3}	1.24×10^{-2}
d	7.50×10^{-4}	1.08×10^{-3}	3.87×10^{-1}	4.14×10^{-1}	6.64×10^{-4}	1.50×10^{-3}
l	1.64×10^{-3}	1.60×10^{-3}	2.69×10^{-1}	5.61×10^{-1}	8.01×10^{-2}	9.96×10^{-2}

to the variability in the nanotube size (d and l), it has a major impact on transverse diffusion coefficient D_{T}. Both D_{L} and D_{T} exhibit an intermediate sensitivity to pore radius R. This is in contrast to the effective rate constant, γ_{eff}, whose variance is dominated by variability in R and, to a significantly smaller extent, by l. Its values are virtually insensitive to θ and d.

3.3.2 Statistical parametrization of the macroscopic model

Uncertainty in values of the pore-scale parameters gives rise to that in values of their macroscopic counterparts. Nonlinearity of the mappings, (3.6) and (3.7), between these two sets of parameters suggests that PDFs of the macroscopic material properties can be nontrivial even when PDFs of the microscopic parameters are. Moreover, the mappings (3.6) and (3.7) imply that even if the pore-scale variables are mutually independent, the macroscopic parameters might be strongly correlated.

We use the kernel density estimators in (3.18) and (3.19) to post-process the $N_{D_{\mathrm{L}}} = N_{D_{\mathrm{T}}} = N_{\gamma_{\mathrm{eff}}} = 10^5$ realizations of the three macroscopic parameters, D_{L},

D_{T} and γ_{eff}. Estimation of the kernel bandwidth with the modified Sheather-Jones method [50] leads to $h_{\mathrm{L}} = 0.0077$, $h_{\mathrm{T}} = 0.0057$ and $h_{\gamma} = 0.0058$ for the KDE in (3.18); and $(h_{\mathrm{L}}, h_{\mathrm{T}}) = (0.0083, 0.0061)$, $(h_{\gamma}, h_{\mathrm{L}}) = (0.0088, 0.0093)$, and $(h_{\gamma}, h_{\mathrm{T}}) = (0.0085, 0.0107)$ for the KDE in (3.19). The resulting (marginal) PDFs, $f_{D_{\mathrm{L}}}(\eta)$, $f_{D_{\mathrm{T}}}(\eta)$ and $f_{\gamma_{\mathrm{eff}}}(\eta)$, are shown in Figure 3.7. All three PDFs are highly asymmetric and exhibit long tails. The non-Gaussianity is, of course, to be expected since these parameters are positive quantities. This finding undermines the long-standing practice of assigning standard (e.g., Gaussian or log-normal) distributions to macroscopic properties of porous media [51, 52, 53, 54, 55].

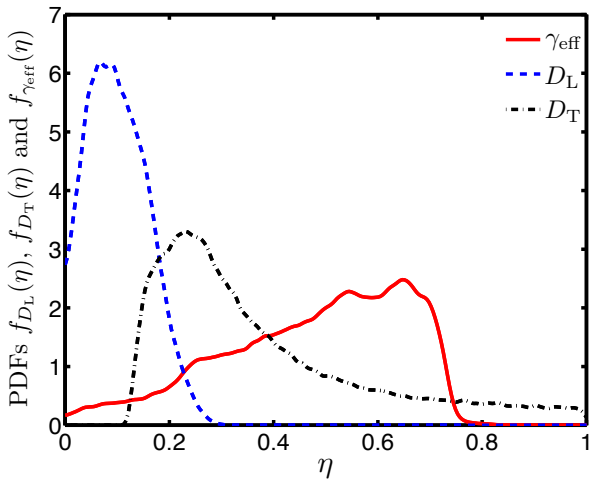

Figure 3.7: Probability density functions $f_{D_{\mathrm{L}}}(\eta)$, $f_{D_{\mathrm{T}}}(\eta)$ and $f_{\gamma_{\mathrm{eff}}}(\eta)$ of the macroscopic material properties, D_{L}, D_{T} and γ_{eff}, respectively. The microscopic parameters $\mathbf{p} = \{R, \theta, d, l\}$ are mutually independent and uniformly distributed.

Joint PDFs, $f_{D_{\mathrm{L}}, D_{\mathrm{T}}}(\eta_{\mathrm{L}}, \eta_{\mathrm{T}})$, $f_{\gamma_{\mathrm{eff}}, D_{\mathrm{T}}}(\eta_{\gamma}, \eta_{\mathrm{T}})$ and $f_{\gamma_{\mathrm{eff}}, D_{\mathrm{L}}}(\eta_{\gamma}, \eta_{\mathrm{L}})$, are shown in Figure 3.8. The three macroscopic parameters, D_{L}, D_{T} and γ_{eff}, are neither statistically independent nor multivariate Gaussian. Like their marginal counterparts in Figure 3.7,

they exhibit multimodality. The longitudinal (D_{L}) and transverse (D_{T}) components of the effective diffusion tensor are positively correlated (the correlation coefficient $\rho_{D_{\mathrm{L}},D_{\mathrm{T}}} = 0.44$), and both are negatively correlated with the effective sorption rate γ_{eff} ($\rho_{\gamma_{\mathrm{eff}},D_{\mathrm{L}}} = -0.50$ and $\rho_{\gamma_{\mathrm{eff}},D_{\mathrm{T}}} = -0.18$).

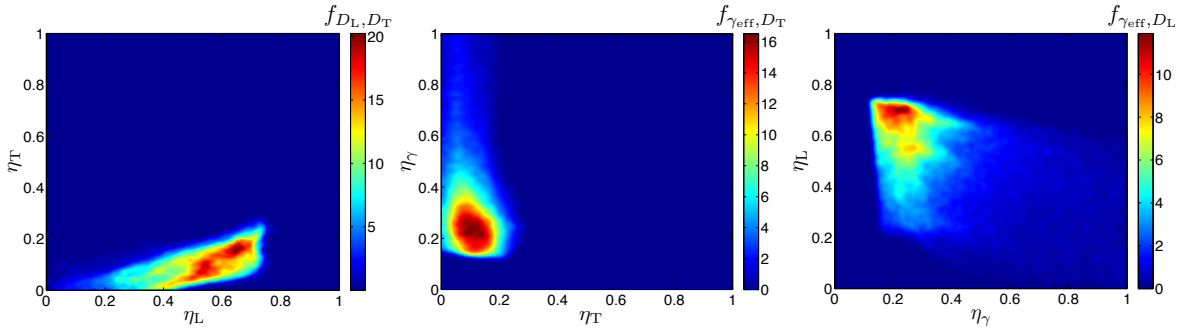

Figure 3.8: From left to right: joint probability density functions $f_{D_{\mathrm{L}},D_{\mathrm{T}}}(\eta_{\mathrm{L}},\eta_{\mathrm{T}})$, $f_{\gamma_{\mathrm{eff}},D_{\mathrm{T}}}(\eta_{\gamma},\eta_{\mathrm{T}})$ and $f_{\gamma_{\mathrm{eff}},D_{\mathrm{L}}}(\eta_{\gamma},\eta_{\mathrm{L}})$ of the macroscopic material properties, D_{L}, D_{T} and γ_{eff}. The microscopic parameters $\mathbf{p} = \{R,\theta,d,l\}$ are mutually independent and uniformly distributed.

3.4 Conclusions

Ubiquitous uncertainty about pore geometry inevitably undermines the veracity of pore- and multi-scale simulations of transport phenomena in porous media. It raises two fundamental issues: sensitivity of effective material properties to pore-scale parameters and statistical parameterization of Darcy-scale models that accounts for pore-scale uncertainty. We treated uncertain geometric characteristics of a hierarchical nanoporous material as random variables to conduct GSA and to derive probabilistic

descriptors of effective diffusion coefficients and effective sorption rate.

Our analysis leads to the following major conclusions.

1. When combined with a probabilistic framework, homogenization-based maps between pore-scale parameters and their Darcy-scale counterparts allow one to estimate global sensitivity of Darcy-scale material properties to geometric characteristics of a material's pore structure and to relate PDFs of pore- and Darcy-scale parameters.

2. For the hierarchical porous medium considered, the effective longitudinal diffusion coefficient (D_{L}) is insensitive to the size of nanotube bridges, while the effective transverse diffusion coefficient (D_{T}) exhibits high sensitivity to this geometric parameter. The longitudinal and transverse components of the effective diffusion tensor are positively correlated (the correlation coefficient $\rho_{D_{\mathrm{L}},D_{\mathrm{T}}} = 0.44$), and both are negatively correlated with the effective sorption rate γ_{eff} ($\rho_{\gamma_{\mathrm{eff}},D_{\mathrm{L}}} = -0.50$ and $\rho_{\gamma_{\mathrm{eff}},D_{\mathrm{T}}} = -0.18$).

3. Multiscale solutions typically depend on the volume fraction. Since derivatives of this macroscopic quantity with respect to the pore space parameters can be evaluated analytically, it may provide a valuable a posteriori interpretation of the GSA results.

4. The proposed approach provides a simple tool that enables a quantitative ranking

of the microstructural parameters.

The simulations reported in this study rely on the simplifying assumption of statistical independence of the uncertain (random) geometric characteristics of hierarchical nanoporous media. In a follow-up study we will obviate the need for this assumption by replacing the variance-based GSA with, e.g., its distribution-based counterpart.

Our analysis is formulated in terms of solute transport diffusing through a fluid-filled pore space, while sorbing to the solid matrix. Yet it is sufficiently general to be applied to other multiscale porous media phenomena that are amenable to homogenization.

Kimoon Um, Xuan Zhang, Markos Katsoulakis, Petr Plechac, and Daniel M. Tartakovsky, "Global sensitivity analysis of multiscale properties of porous materials", *Journal of Applied Physics*, 123, 075103(2018).

Chapter 4

Probabilistic graphical models and multi-scale porous media

Our primary objective is to bring a Bayesian network perspective to the modeling of multiscale porous media. In particular, we will build a Probabilistic Graphical Model (PGM) for pore scale parameters and incorporate this into a full Bayesian network(statistical model) for the multiscale porous media system described in chapter 3. PGMs, for example depicted in fig.4.1 to fig.4.3, provide a rich framework for encoding distributions over large, complex domains of interacting random variables i.e. parameter space in our application of interest [56][57][58]. If the structure of the PGM is a directed acyclic graph (also known as a Bayesian network) then the model provides a factorization for the joint probability distribution of random variables that respects

correlations. Constructing a PGM for pore scale parameters is a novel approach to modeling multiscale porous media that will allow us to break down the stochastic modeling and statistical inference tasks into smaller, controllable parts enabling us to:

1. Build systematically informed parameter priors that include physical constraints and/or correlations.

2. Carry out global sensitivity analysis and (traditional) uncertainty quantification.

3. Build systematically random PDE models at the Darcy scale, which are informed by pore-scale parameters, constraints, and uncertainties.

Overall, we believe that PGMs provide a systematic way of building a complete predictive model, including forward physical models, transitions between scales (e.g. homogenization) and uncertainties in parameters, mechanisms and parameter or model constraints.

After introducing the full Bayesian network for our multiscale porous media in 4.1, we focus on a particular component: modeling of the pore scale parameters. Presently, we provide two examples based on hierarchical pore scale parameters,

1. with independent priors following chapter 3 and

2. with correlations induced by geometrical constraints,

and illustrate how to incorporate these into the full Bayesian network. Our general goals for this work are:

a. build Random PDE models by constructing corresponding Darcy parameters;

b. compare findings and role of constraints/correlations;

c. other priors, that incorporate computational data and experiments.

4.1 PGMs for multiscale porous media

Presently, we introduce a framework for treating the statistical model for the multiscale porous media system outlined in chapter 3 and follow every terminologies(definitions) and hierarchical pore structure in figure 3.1. Following the description in chapter 3, the key components of the full statistical model are:

1. $\boldsymbol{\Theta}$, a random vector of parameters related to the pore-scale geometry;

2. $\boldsymbol{X}$, a random field related to the closure equations in (3.7b)) to (3.7f) obtained via homogenization of the pore-scale physical model; and

3. U, a random field related to the macroscopic Darcy flow equations in (3.5), (3.6), and (3.7a).

A Bayesian network formulation for the full statistical model that describes the relationships among these three components($\boldsymbol{\Theta}$), $\boldsymbol{X}$, and U) is given in figure 4.1.

The model output U depends on the distribution of $\boldsymbol{X}$ since the Darcy-scale solute u depends on the closure variable $\boldsymbol{\chi}$. In turn, we observe that $\boldsymbol{X}$ depends on the distribution of $\boldsymbol{\Theta}$ since $\boldsymbol{\chi}$ depends on $\boldsymbol{p}$. Roughly, the variable $\boldsymbol{\Theta}$ is related to the pore-scale geometry, U is related to the Darcy scale, and $\boldsymbol{X}$ is related to the homogenization that links the two scales. We observe that the network structure in figure 4.1 is directed, indicating that there is no communication between the problem scales.

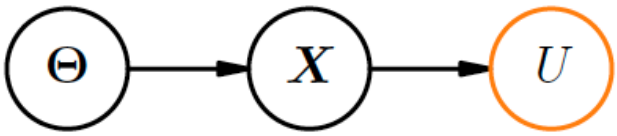

Figure 4.1: A Bayesian network describing the components of the full statistical model P in (4.3) for the multi-scale porous media system takes into account the joint distribution $P(\boldsymbol{\Theta})$ of the parameters, the distribution $P(\boldsymbol{X} \mid \boldsymbol{\Theta})$ of the closure variable, and the output distribution $P(U \mid \boldsymbol{X})$ of the Darcy solute. Cf. with the PGMs in figure 4.2, figure 4.3 which replace the simple $\boldsymbol{\Theta}$ component above with additional structure.

For the network in figure 4.1, the full statistical model possesses the following form. Let $P(\boldsymbol{p})$ denote the joint distribution of the parameters and for simplicity we assume the models for $\boldsymbol{X}$ and U are known, i.e. since $\boldsymbol{\chi}$ and u solve deterministic equations that uncertainty enters only through the parameters. Then the distribution

of $\boldsymbol{X}$ is given by the trivial distribution

$$P(\boldsymbol{X} \mid \boldsymbol{\Theta}) = \delta_{\boldsymbol{X}}(\boldsymbol{X} - \boldsymbol{\chi}(\boldsymbol{\xi}, t; \boldsymbol{\Theta})) \tag{4.1}$$

where $\boldsymbol{\chi}$ solves (3.7b) to (3.7f) given a sample $\boldsymbol{\Theta} = \boldsymbol{p}$. Similarly, the distribution of U is given by

$$P(U \mid \boldsymbol{X}) = \delta_U(U - u(\boldsymbol{x}, t; \boldsymbol{X})) \tag{4.2}$$

where u solves (3.5), (3.6), (3.7a) given a sample $\boldsymbol{X} = \boldsymbol{\chi}$. Then the full statistical model P is given by

$$\begin{aligned} P :=& P(\boldsymbol{\Theta}, \boldsymbol{X}, U) = P(U \mid \boldsymbol{X})\ P(\boldsymbol{X} \mid \boldsymbol{\Theta})\ P(\boldsymbol{\Theta}) \\ =& \delta_U(U - u(\boldsymbol{x}, t; \boldsymbol{X}))\ \delta_{\boldsymbol{X}}(\boldsymbol{X} - \boldsymbol{\chi}(\boldsymbol{\xi}, t; \boldsymbol{\Theta}))\ P(\boldsymbol{\Theta})\,. \end{aligned} \tag{4.3}$$

The representation in (4.3) enables uncertainty quantification. The traditional uncertainty quantification perspective involves strategies for sampling the model P above, such as generalized polynomial chaos (gPC) and Monte Carlo methods(MC). The sampled model is then used for critical uncertainty quantification tasks such as global sensitivity analysis. These traditional uncertainty quantification methods rely on the form of P being known and deal with how changes to the distribution affect changes to forward (physical) model outputs/quantities of interest. The model-form uncertainty quantification tasks deal with providing robust and tight bounds on the error in a quantity of interest between two different models for P. In this sense, the model-form UQ tasks allow us to answer questions about the impact that various

modeling choices related to P will have on our quantities of interest and are key to the support of various decision tasks.

4.1.1 First simple case: full statistical model with uniform priors

The analysis in chapter 3 for the simple hierarchical nanopore geometry in figure 3.1 assumes independent uniform priors for each of the pore scale parameters $\boldsymbol{p} = \{R, \theta, l, d\}$. For $\boldsymbol{\Theta} = (\Theta_1, \ldots, \Theta_n)$ (in particular with $n = 4$ for the given $\boldsymbol{p}$) we assume that the Θ_i are independent, that is, we assume

$$\Theta_i \amalg \Theta_j \qquad \Longleftrightarrow \qquad P(\Theta_i, \Theta_j) = P(\Theta_i)P(\Theta_j)\,,$$

for all $i, j = 1, \ldots, n$ such $i \neq j$. Then we have that the joint distribution for $\boldsymbol{\Theta}$ factors into the product of the priors

$$P(\boldsymbol{\Theta}) = \prod_{i=1}^{n} P(\Theta_i)\,. \tag{4.4}$$

The full statistical model for P in (4.3) is given by

$$P_0 := \delta_U(U - u(\boldsymbol{x}, t; \boldsymbol{X}))\; \delta_{\boldsymbol{X}}(\boldsymbol{X} - \boldsymbol{\chi}(\boldsymbol{\xi}, t; \Theta_1, \ldots, \Theta_n)) \prod_{i=1}^{n} P(\Theta_i) \tag{4.5}$$

and in this case the Bayesian network has the special form given in figure 4.2. In figure 4.2, the independent priors assumption on $\boldsymbol{\Theta} = (\Theta_1, \ldots, \Theta_n)$ leads to a flat structure with each Θ_i, $i = 1, \ldots, n$, pointing at $\boldsymbol{X}$. This independence assumption

does not take into account correlations between the pore scale parameters $\boldsymbol{\Theta}$ that are induced by geometrical constraints. As a second simple case, we consider correlations imposed by geometrical constraints by adding more complexity to the structure of the priors for $\boldsymbol{\Theta}$.

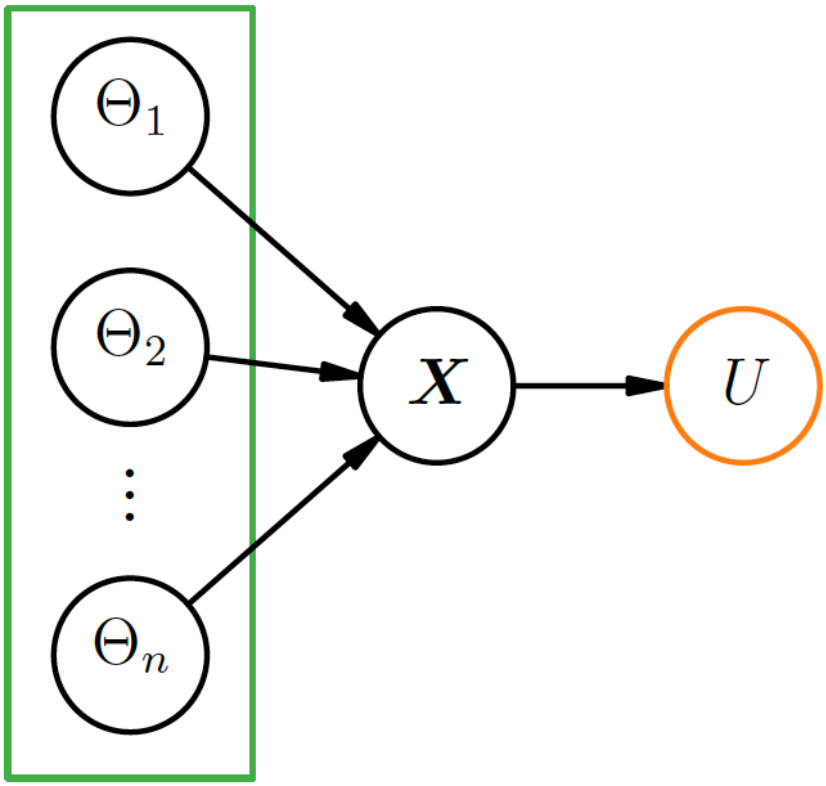

Figure 4.2: A Bayesian network describing the components of the full statistical model under the assumption of independent priors on $\boldsymbol{\Theta} = (\Theta_1, \ldots, \Theta_n)$. Cf. the flat structure of the $\boldsymbol{\Theta}$ component in the model above to the rich structure of the Bayesian network in 4.3 that captures $\boldsymbol{\Theta}$ correlations.

4.1.2 Second simple case: correlations arising from geometrical constraints

One possible PGM for the hierarchical pore scale parameters $\boldsymbol{p} = \{R, \theta, l, d\}$ is as follows. For each of the parameters $p \in \boldsymbol{p}$, we fix hyperparameters $\{p_-, p_+\}$ corresponding to upper and lower bounds on p. Then one chooses a subset of independent parameters, e.g. $\{R, \theta\}$, and assumes independent uniform priors, that is

$$\Theta_R \mid (R_-, R_+) \sim \text{Uniform}(R_-, R_+) \quad \text{and} \quad \Theta_\theta \mid (\theta_-, \theta_+) \sim \text{Uniform}(\theta_-, \theta_+)\,.$$

The physical geometry implicitly constrains the remaining dependent parameters l and d:

$$l \geq \max\{2R - 2R\sin\theta, l_-\} \tag{4.6}$$

and

$$d \leq \min\{2R\cos\theta, d_+\}\,. \tag{4.7}$$

Thus, the distribution of Θ_l and Θ_d depends on the distribution of Θ_R and Θ_θ.

These choices also fix other aspects of the pore scale geometry such as the unit cell length x, the unit cell height[1] y, and nanotube/mesopore overlap ϵ (i.e. $\epsilon = \frac{1}{2}|l - l_s|$ where l is the length of the nanotube as measured at the center and l_s as measured at the side). Although the parameters x, y, and ϵ are redundant in the sense that the do not provide additional information to that already contained in (R, θ, l, d), these

[1] Compare to a and b in chapter 3: $x = a/2$ and $y = b$.

parameters might play a role in sensitivity analysis. For example the parameter ϵ, which depends on R, l, and θ is related to the sharpness of the inward facing angle in the domain. This parameter also plays a role in the specification of the numerical method. Choosing which parameter "directions" are most sensitive to perturbations via principal component analysis vs basis directions. It is important from the perspective of global sensitivity analysis.

Given these geometric constraints, it is more appropriate to assume a distribution for Θ_l and Θ_d conditioned on an observation Θ_R, Θ_θ. That is, the conditional density of Θ_l given Θ_R, Θ_θ is

$$\Theta_l \mid (\Theta_R, \Theta_\theta, l_-, l_+) \sim \text{Uniform}(\max\{2R - 2R\sin\theta, l_-\}, l_+) \tag{4.8}$$

and Θ_d given Θ_R, Θ_θ, is

$$\Theta_d \mid (\Theta_R, \Theta_\theta, d_-, d_+) \sim \text{Uniform}(d_-, \min\{2R\cos\theta, d_+\})\,. \tag{4.9}$$

A pictorial representation of the causality and correlations discussed above is given by the directed graph in figure 4.3. In figure4.3, fixed hyperparameter values are represented by closed dots, independent variables are flagged with red, and dependent variables are flagged with blue. There are edges between Θ_R and Θ_l, Θ_θ and Θ_l, Θ_R and Θ_d, and Θ_θ and Θ_d indicating a correlation between these parameters (where the conditional relationship is given by the direction of the arrow). The absence of edges

between Θ_R and Θ_θ indicates the independence

$$\Theta_R \amalg \Theta_\theta$$

and the absence of edges between Θ_l and Θ_d indicates conditional independence

$$\Theta_l \amalg \Theta_d \mid (\Theta_R, \Theta_\theta) \ ,$$

(i.e., the latter quantity indicates that the conditional density factors into the product of the marginals).

Using the relationships encoded in 4.3, we have that the joint distribution $P(\boldsymbol{\Theta})$ is given by

$$\begin{aligned} P(\boldsymbol{\Theta}) =& P(\Theta_l, \Theta_d \mid \Theta_R, \Theta_\theta) P(\Theta_R, \Theta_\theta) \\ =& P(\Theta_l \mid \Theta_R, \Theta_\theta) P(\Theta_d \mid \Theta_R, \Theta_\theta) P(\Theta_R) P(\Theta_\theta) \, . \end{aligned} \tag{4.10}$$

(c.f. the joint density assuming independent priors in 4.4). Incorporating this component into the full statistical model 4.3, we obtain the expression

$$\begin{aligned} P_1 :=& \delta_U(U - u(\boldsymbol{x}, t; \boldsymbol{X})) \ \delta_{\boldsymbol{X}}(\boldsymbol{X} - \boldsymbol{\chi}(\boldsymbol{\xi}, t; \boldsymbol{\Theta})) \ P(\Theta_l \mid \Theta_R, \Theta_\theta) \\ & \cdot P(\Theta_d \mid \Theta_R, \Theta_\theta) P(\Theta_R) P(\Theta_\theta) \, , \end{aligned} \tag{4.11}$$

which describes the statistical model for the full multiscale system with the correlation structure in figure 4.3 assuming the models for U and $\boldsymbol{X}$ are known.

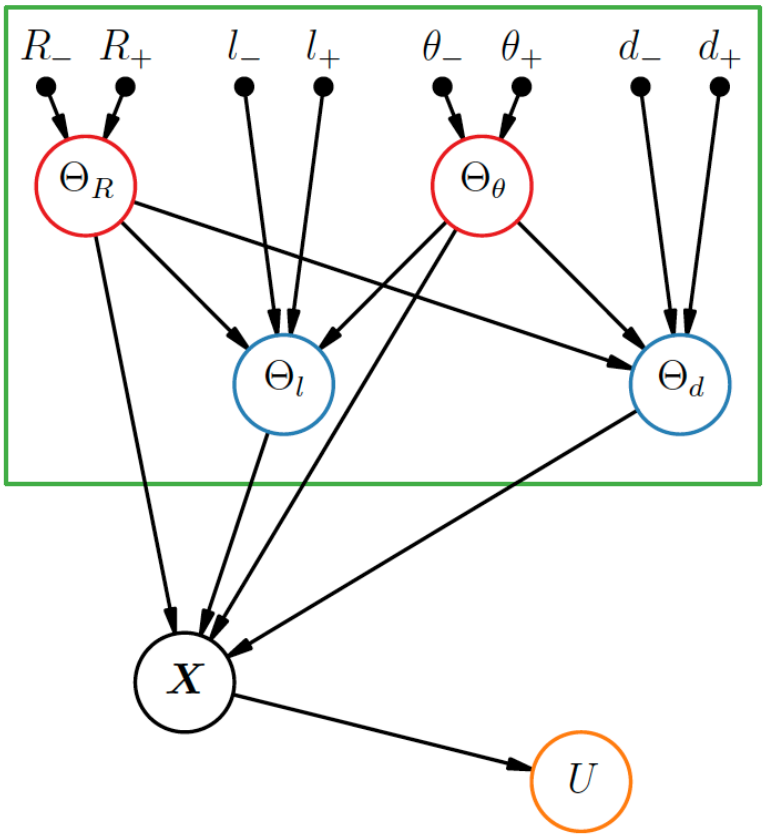

Figure 4.3: A PGM for pore scale geometry that encodes the correlations among the distribution for pore scale parameters $\boldsymbol{\Theta} = \{\Theta_R, \Theta_\theta, \Theta_l, \Theta_d\}$. Note that $\Theta_R \amalg \Theta_\theta$ and $\Theta_l \amalg \Theta_d \mid (\Theta_R, \Theta_\theta)$. The rich structure above encodes correlations among the $\boldsymbol{\Theta}$ that are absent in the model represented in 4.2.

4.1.3 Unknown model for the Darcy scale process

In chapter 3, the interest is in analyzing a quantity of interest $D_L := \mathbf{D}_{\text{eff}}^{11}$, a functional of the macroscopic Darcy parameters $\{\mathbf{D}_{\text{eff}}(\boldsymbol{p}), \gamma_{\text{eff}}(\boldsymbol{p})\}$. Instead of being a statistic of the forward model output, the goal functional was a kernel density estimator f for D_L that then depends on the joint distribution of the pore-scale parameters $\boldsymbol{p}$. In this case, the distribution of the quantity of interest is not the trivial distribution

(4.2) but is instead a kernel density estimator which has some error (a distribution). In particular, the network in figure 4.3 yields the model:

$$P_3 := f(D_L \mid \boldsymbol{\Theta}) = f(D_L \mid \boldsymbol{X})\ \delta_{\boldsymbol{X}}(\boldsymbol{X} - \boldsymbol{\chi}(\boldsymbol{\xi}, t; \boldsymbol{\Theta}))\ P(\Theta_l \mid \Theta_R, \Theta_\theta)$$

$$\cdot\, P(\Theta_d \mid \Theta_R, \Theta_\theta) P(\Theta_R) P(\Theta_\theta)\,.$$

This model can be sampled using traditional uncertainty quantification methods and in particular the variance of this density can then be analyzed using the techniques in chapter 3.

One might play a similar game with the closure variable: the error in the homogenization can be included by putting a distribution on $\boldsymbol{X}$ that is not trivial, i.e. by replacing (4.1) with some distribution that captures the error in the homogenization.

4.1.4 Rosenblatt transform

We sample our parameters uniformly at random from a hypercube. Rosenblatt's transformation [59] is useful; it transforms the problem of sampling a general joint distribution into the problem of sampling a vector of independent Uniform$(0, 1)$ random variables.

Let $(X_1, \ldots, X_k)$ be a random vector with continuous joint cumulative distribution function $F(x_1, \ldots, x_k)$. Define a transformation $\mathcal{T}x = \mathcal{T}(x_1, \ldots x_k) = (z_1, \ldots, z_k) =$

z given by

$$
\begin{aligned}
z_1 &= P(X_1 \leq x_1) = F_1(x_1)\,, \\
z_2 &= P(X_2 \leq x_2 \mid X_1 = x_1) = F_{2|1}(x_2 \mid x_1)\,, \\
&\vdots \\
z_k &= P(X_k \leq x_k \mid X_{k-1} = x_{k-1}, \ldots, X_1 = x_1) = F_{k|k-1,\ldots,1}(x_k \mid x_{k-1}, \ldots, x_1)\,,
\end{aligned}
$$

where $F_{i|j}$ is the conditional distribution of X_i given X_j. Then the random vector $Z := \mathcal{T}(X)$ is uniformly distributed on the k-dimensional hypercube (i.e. $Z_1, \ldots, Z_k$ are IID Uniform$(0,1)$).

For our random vector of parameters $\mathbf{\Theta} = (\Theta_R, \Theta_\theta, \Theta_l, \Theta_d)$, we note that given the model in 4.3 the Rosenblatt transform $\mathcal{T}$ takes the form

$$
\begin{aligned}
z_1 &= F_R(x_1)\,, \\
z_2 &= F_{\theta|R}(x_2 \mid x_1) = F_\theta(x_2)\,, \qquad (\text{since } \Theta_R \amalg \Theta_\theta)\,, \\
z_3 &= F_{l|R,\theta}(x_3 \mid x_2, x_1)\,, \\
z_4 &= F_{d|l,R,\theta}(x_4 \mid x_3, x_2, x_1) = F_{d|R,\theta}(x_4 \mid x_2, x_1)\,, \qquad (\text{since } \Theta_d \amalg \Theta_l \mid \Theta_R, \Theta_\theta)\,.
\end{aligned}
$$

Thus

$$
\begin{aligned}
\mathcal{T}(\mathbf{\Theta}) =& \mathcal{T}(\Theta_R, \Theta_\theta, \Theta_l, \Theta_d) \\
&= \big(F_R(\Theta_R),\ F_\theta(\Theta_\theta),\ F_{l|R,\theta}(\Theta_l \mid \Theta_R = R, \Theta_\theta = \theta),\ F_{d|R,\theta}(\Theta_d \mid \Theta_R = R, \Theta_\theta = \theta)\big)
\end{aligned}
$$

where (since each of the cumulative distribution functions above corresponds to a

uniform distribution) the components of the random vector are given by the variables

$$
\begin{aligned}
Z_1 := F_R(\Theta_R) &= \frac{\Theta_R - R_-}{R_+ - R_-}\,, \\
Z_2 := F_\theta(\Theta_\theta) &= \frac{\Theta_\theta - \theta_-}{\theta_+ - \theta_-}\,, \\
Z_3 := F_{l|R,\theta}(\Theta_l) &= \frac{\Theta_l - \max\{(2R - 2R\sin\theta), l_-\}}{l_+ - l_-}\,, \\
Z_4 := F_{d|R,\theta}(\Theta_d) &= \frac{\Theta_d - d_-}{\min\{2R\cos\theta, d_+\} - d_-}\,.
\end{aligned}
$$

This transforms the sampling problem into the problem of sampling a vector $Z = (Z_1, Z_2, Z_3, Z_4)$ of independent Uniform$(0, 1)$ random variables. In particular, we are interested in a quantity of interest $Y = \mathcal{M}(\Theta)$ where $\mathcal{M}$ is the (forward) model with random input Θ. Then the compositional model $Y = (\mathcal{M} \circ \mathcal{T}^{-1})(Z)$ provides a means of computing since the statistics of the output of $\mathcal{M} \circ \mathcal{T}^{-1}$ in response to Z are identical to the statistics of the output of $\mathcal{M}$ in response to Θ [60].

4.1.5 Recipe for using this method with Monte Carlo sampling

1. Specify upper and lower limits on the parameters,

   i.e. fix: $R_-, R_+, \theta_-, \theta_+, l_-, l_+, d_-, d_+$.

2. Sample IID Uniform$(0, 1)$ random variables Z_1, Z_2, Z_3, Z_4 .

3. Use inverse transform $\Theta = \mathcal{T}^{-1}(Z)$ to obtain a sample values R, θ, l, d for each of

$\Theta_R, \Theta_\theta, \Theta_l, \Theta_d$, i.e.:

(a) $R := Z_1(R_+ - R_-) + R_-$,

(b) $\theta := Z_2(\theta_+ - \theta_-) + \theta_-$,

(c) $l := Z_3(l_+ - l_-) + \max\{(2R - 2R\sin\theta),\, l_-\}$,

(d) $d := Z_4(\min\{2R\cos\theta,\, d_+\} - d_-) + d_-$.

4. Run forward model using sample values R, θ, l, d; these sample are drawn from the appropriate joint distribution with correlations.

5. Conduct uncertainty quantification analysis.

For the (isoprobabilistic) transform $\mathcal{T}$, the statistics of the quantity of interest with respect to the compositional model $\mathcal{M} \circ \mathcal{T}^{-1}$ with input Z should match the statistics with respect to the original model $\mathcal{M}$ with input Θ.

4.2 Results

We consider the hierachical nanoporous material shown in Fig. 3.1. The independent random variable of the pore-scale parmeter $\mathbf{p}$ in chapter 3 is shown in (4.3). And we take account of the correaltion of pore-scale parameter (4.7) to (4.6) and rebuild it in (4.11) using a Probabilistic Graphical Model. But the input parameters

are given uniform random distribution ($0 \leq Z \leq 1$) by Rosenblatt transformation explained in 4.1.4. We use (3.17) and corresponding probability density functions(PDF) using a kernel density estimator(KDE) described in (3.18) and (3.19).

4.2.1 Comparison of independent inputs and uncorrelated inputs

Input parameters ($\mathbf{p}$) in pore-scale reported in table 4.1 brings about macroscopic counterpart. We compare the macroscopic values by probabilistic graphical model with those reported in chapter 3. We use the Kernel Distribution Estimator(KDE) in (3.18) and (3.19) and show the results in figure 4.4 and in figure 4.7. We post-process the 10^5 realizations of three macroscopic parameters, D_{L}, D_{T}, and γ_{eff} from the PCEs in (3.17) and use KDE. Estimation of the kernel bandwidth with the modified Sheather-Jones method [50] indicates $h_{\mathrm{L}} = 0.0058$, $h_{\mathrm{T}} = 0.0012$, and $h_{\gamma} = 8.6741 \times 10^{-4}$ for the KDE in (3.18) and (h_{L}, h_{T}) = (0.0049, 0.0023), (h_{T}, h_{γ}) = (0.0025, 0.0015), and (h_{γ}, h_{L}) = (0.0020, 0.0046) for the KDE in (3.19). The comparing results of marginal PDF are shown in figure 4.4. They behaves similar

Table 4.1: Range of input parameter to make comparion of results between the independent input parameters and correlated input parameters

	$R(nm)$	$\theta(rad)$	$d(nm)$	$l(nm)$
Max.	60	0.7	8	18
min.	10	0.07	4	8

trends but PGM model shows more narrow and sharp distribution. This results shows very simple geometrical correlation(constraints) brings about changes of the Darcy scale properties.

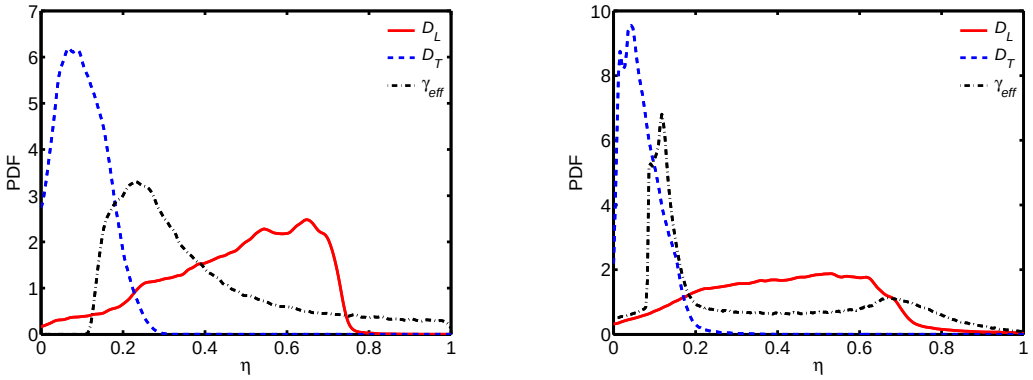

Figure 4.4: PDFs of $f_{D_{\mathrm{L}}}(\eta)$, $f_{D_{\mathrm{T}}}(\eta)$, and $f_{\gamma}(\eta)$. Left graph : PDFs from independent input parameters, right graph : PDFs from correlated input parameters.

Joint PDFs are shown in figure 4.7. These joint PDFs also show similar distribution to independent random value in pore-scale, that is, effective diffusion in longitudinal direction(D_{L}) and transverse direction(D_{T}) are positively correlated, and both are negatively correlated with the effective sorption rate(γ_{eff}). Joints PDFs also have narrow distribution, particularly in $f_{D_{\mathrm{T}},D_{\gamma}}$. It is concentrated very small range of η_{T} and η_{γ} and even seen as optimized property of Darcy-scale.

Table 4.2: Range of input parameters from pore-scale. Maximum value and minmum value is corresponding with described values in figure 4.3(R_+, R_-, θ_+, θ_-, d_+, d_-, l_+, l_-)

	$R(nm)$	$\theta(rad)$	$d(nm)$	$l(nm)$
Max.	60	0.05π	60	60
min.	10	0.4π	5	1

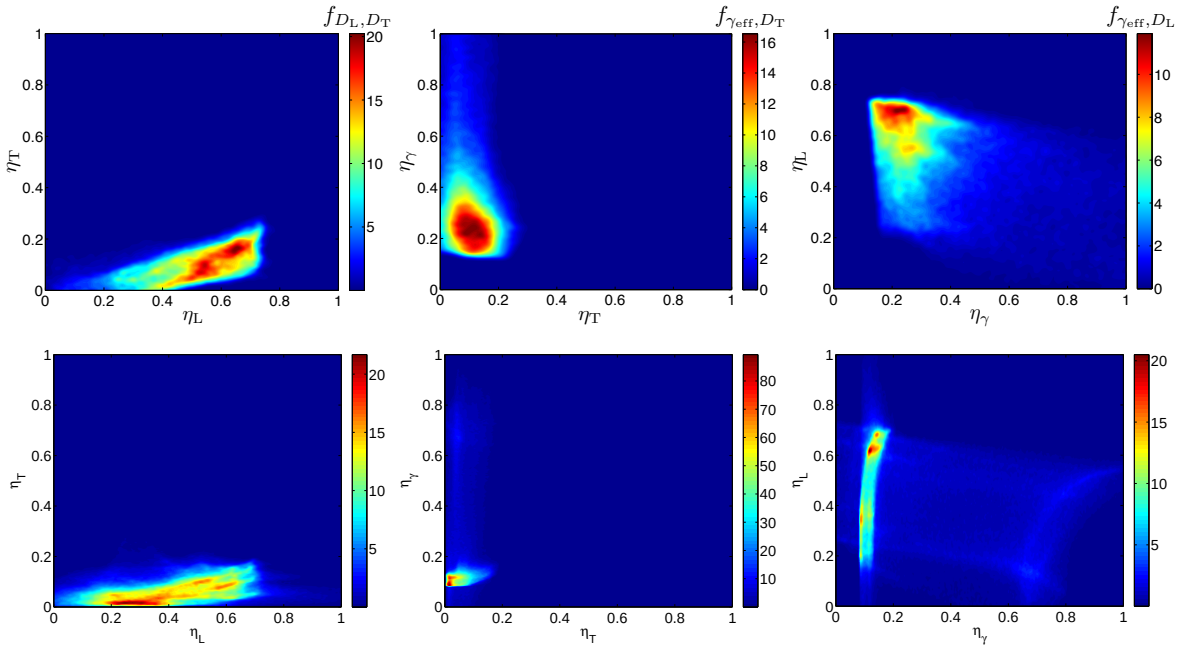

Figure 4.5: From left to right: joint probability density functios $f_{D_{\mathrm{L}},D_{\mathrm{T}}}(\eta_{\mathrm{L}},\ \eta_T)$, $f_{\gamma_{eff},D_{\mathrm{T}}}(\eta_\gamma,\ \eta_T)$, $f_{\gamma_{eff},D_{\mathrm{L}}}(\eta_\gamma,\ \eta_L)$ of macroscopic material properties, D_{L}, D_{T}, and γ_{eff}. Upper row : independent input parameters of $\mathbf{p}$ and below row : correlated input parameters by PGM.

4.2.2 PGM with wider range of input parameters

Uncertainty quantification

The greatest benefit of correlation input is that the correlations coming from the geometric factors(constraints) are considered in figure 4.3. And the interval is reported in Table 4.2 relatively larger interval for d and l to see the effect of correlation of input parameters. We analyze PGM model following described in 4.1.5 and post-process the 10^5 realizations of three macroscopic parameters, D_{T}, D_{L}, and γ_{eff} from the polynomial chaos expansion and kernel density estimator.

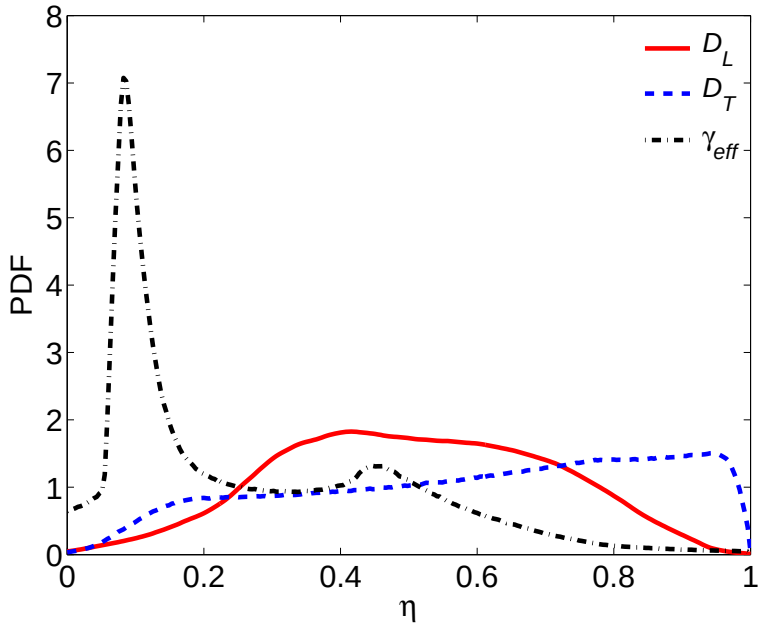

Figure 4.6: $f_{D_{\mathrm{L}}}(\eta)$, $f_{D_{\mathrm{T}}}(\eta)$, and $f_{\gamma}(\eta)$ of the macroscopic material properties, D_{L}, D_{T}, and γ_{eff} respectively. Microscopic parameters are correlated and following the interval shown in table 4.2.

The estimated kernel density bandwidths by the modified Shearther-Jones method [50] are $h_{\mathrm{L}} = 0.0065$, $h_{\mathrm{T}} = 0.0016$, and $h_{\gamma} = 0.0011$ for the KDE in (3.18) and $(h_{\mathrm{L}}, h_{\mathrm{T}}) = (0.0080, 0.0049)$, $(h_{\mathrm{T}}, h_{\gamma}) = (0.0038, 0.0022)$, and $(h_{\gamma}, h_{\mathrm{L}}) = (0.0015, 0.0042)$ for the KDE in (3.19). The comparing results of marginal PDF are shown in figure 4.6. $f_{D_{\mathrm{L}}}$, and $f_{\gamma_{eff}}$ behave similar tendency though wider interval of microscopic input parameter(d, l) but $f_{D_{\mathrm{T}}}$ trends different. Microscopic parameter d influences most to macroscopic parameter D_{T} and nanoporous geometry could have wider interval of it without breaking geometric limits through probabilistic graphical model.

Joint probability density functions, $f_{D_{\mathrm{L}},D_{\mathrm{T}}}(\eta_{\mathrm{L}}, \eta_{\mathrm{T}})$, $f_{\gamma_{eff},D_{\mathrm{L}}}(\eta_{\gamma}, \eta_{\mathrm{L}})$, and $f_{\gamma_{eff},D_{\mathrm{T}}}(\eta_{\gamma}, \eta_{\mathrm{T}})$, are shown in figure 4.7. $f_{D_{\mathrm{L}},D_{\mathrm{T}}}(\eta_{\mathrm{L}}, \eta_{\mathrm{T}})$ shows highly complex behavior though $f_{\gamma_{eff},D_{\mathrm{T}}}(\eta_{\gamma}, \eta_{\mathrm{T}})$ are biased(concentrated).

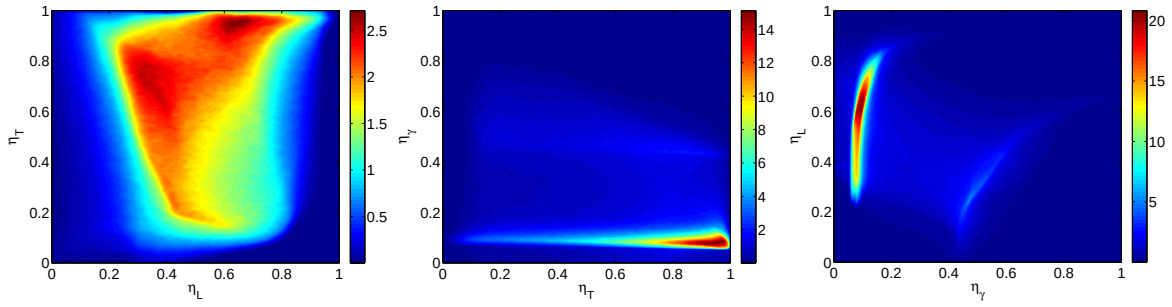

Figure 4.7: From to to bottom: joint probability density functions $f_{D_{\mathrm{L}},D_{\mathrm{T}}}(\eta_{\mathrm{L}}, \eta_T)$, $f_{\gamma_{eff},D_{\mathrm{T}}}(\eta_{\gamma}, \eta_T)$, $f_{\gamma_{eff},D_{\mathrm{L}}}(\eta_{\gamma}, \eta_L)$ of macroscopic material properties, D_{L}, D_{T}, and γ_{eff} from the correlated input parameters reported in table 4.2.

4.3 Summary and discussion

We build Random PDE models by constructing corresponding Darcy parameters (run simulations using P_1 model) and the correlations in the pore-scale parameter enables us to understanding of behaviors of effective diffusion coefficient in the transverse direction. In previous analysis, it is difficult to see the behavior of D_T because of geometrical constraints once we use uniformly distributed pore-scale parameters. We see that the diffusion coefficients are highly non-linear and very complex coming from geometrical non-linearity.

One direction could be, given the structure of the PGM, to consider a case where correlations are inferred from some data set (simulated data comprising measurements). Another direction: in general, the parameters that describe the geometry themselves might be unknown (and possibly high dimensional) and the parameters and their correlations might be obtained from a machine learning technique using experimental (image) data.

Um, K., E. Hall, M. Katsoulakis, and D. M. Tartakovsky, "Probabilistic graphical models and multiscale porous media", submitted

Chapter 5

Conclusion

This dissertation leads to the following major conclusions:

1. In complex biological problems, wide range of spatial and/or temporal conditions brings about the necessities of multi-scale simulation. Here we develop hybrid algorithm to implement of different scale for chemotaxis-motility-reaction problem. Three different phenomenons are controlled by operator-splitting method. Random motility is described by stochastic method using Brownian motion and reaction is depicted by Gillespie multi-particle method considering the chemical master equation. Chemotaxis which is influenced by the concentration and the gradient of concentration of chemo-attractants acquired by continuum scale calculation could be described in hybrid method. The cell Pèclet number is calculated for each leukocyte or bacteria particle to determine its dominated dominated

scheme(diffusion– or advection–dominated scheme). Also Damköhler number is taken account to determine proper time step. Hybrid algorithm in different scale of species(chemattractants, bacteria, and leukocytes) is validated by comparing continuum scale model with error analysis and it is turned out solid algorithm in the aspect of speed and accuracy.

2. Multiscale simulation in pore-scale geometric structure and Darcy-scale material properies is conducted for material design. We can see the probabilistic relation though the geometric parameters in the pore-scale is independent. Darcy-scale properties, effective diffusion coefficients and effective sorption rate are calculated by upscaling with closure and randomness comes from uniform distribution of pore-scale input parameters. Polynomial chaos expansion about Darcy-scale properties drives the probability density function and the joint probability density function using kernel density estimator and these shows the relationship between the Darcy-scale properties. Also global sensitivity analysis based on Sobol's indices and total indices gives the guideline of material design by showing the ranking of the most effective influence. The ranks indicate the effectiveness of pore-scale parameters to Darcy-scale parameters.

3. In real experiments, the intrinsic constraints(correlations) limits the material design. Probabilistic graphical methods helps to consider the correlation in the

pore-scale parameters and Rosenblatt transformation and inverse transformation makes these correlations handled in uniform distribution. We validate PGM using same interval of input parameter. Larger input range shows different relationship in Darcy-scale parameters and this comes from the correlation as well. Geometric correlations produce more condensed range in joint probabilistic density function and these results suggests most probable output(Darcy-scale parameters) under given interval of input parameters(pore-scale).

Bibliography

[1] Brian Munsky and Mustafa Khammash. The finite state projection algorithm for the solution of the chemical master equation. *The Journal of chemical physics*, 124(4):044104, 2006.

[2] Daniel T Gillespie. A rigorous derivation of the chemical master equation. *Physica A: Statistical Mechanics and its Applications*, 188(1-3):404–425, 1992.

[3] Barbara Bravi and Giuseppe Longo. The unconventionality of nature: biology, from noise to functional randomness. In *International Conference on Unconventional Computation and Natural Computation*, pages 3–34. Springer, 2015.

[4] TaiJung Choi, Mano Ram Maurya, Daniel M Tartakovsky, and Shankar Subramaniam. Stochastic operator-splitting method for reaction-diffusion systems. *The Journal of chemical physics*, 137(18):184102, 2012.

[5] J. Bakarji and D. M. Tartakovsky. On the use of reverse brownian motion to accelerate hybrid simulations. *J. Comput. Phys.*, 334:68–80, 2017.

[6] S. Taverniers, A. Y. Pigarov, and D. M. Tartakovsky. Conservative tightly-coupled simulations of stochastic multiscale systems. *J. Comput. Phys.*, 313:400–414, 2016.

[7] T.-J. Choi, M. R. Maurya, D. M. Tartakovsky, and S. Subramaniam. Stochastic hybrid modeling of intracellular calcium dynamics. *J. Chem. Phys.*, 133(16):165101, 2010.

[8] Evelyn F Keller and Lee A Segel. Model for chemotaxis. *Journal of theoretical biology*, 30(2):225–234, 1971.

[9] Thomas Hillen and Kevin J Painter. A users guide to pde models for chemotaxis. *Journal of mathematical biology*, 58(1-2):183, 2009.

[10] Wolgang Alt. Biased random walk models for chemotaxis and related diffusion approximations. *Journal of mathematical biology*, 9(2):147–177, 1980.

[11] Robert T Tranquillo and Douglas A Lauffenburger. Definition and measurement of cell migration coefficients. In *Biological Motion*, pages 475–486. Springer, 1990.

[12] Gilbert Strang. On the construction and comparison of difference schemes. *SIAM Journal on Numerical Analysis*, 5(3):506–517, 1968.

[13] Willem Hundsdorfer and Jan G Verwer. *Numerical solution of time-dependent advection-diffusion-reaction equations*, volume 33. Springer Science & Business Media, 2013.

[14] J Vidal Rodríguez, Jaap A Kaandorp, Maciej Dobrzyński, and Joke G Blom. Spatial stochastic modelling of the phosphoenolpyruvate-dependent phosphotransferase (pts) pathway in escherichia coli. *Bioinformatics*, 22(15):1895–1901, 2006.

[15] Brian E Farrell, Ronald P Daniele, and Douglas A Lauffenburger. Quantitative relationships between single-cell and cell-population model parameters for chemosensory migration responses of alveolar macrophages to c5a. *Cell motility and the cytoskeleton*, 16(4):279–293, 1990.

[16] Subrahmanyan Chandrasekhar. Stochastic problems in physics and astronomy. *Reviews of modern physics*, 15(1):1, 1943.

[17] Sally H Zigmond. Ability of polymorphonuclear leukocytes to orient in gradients of chemotactic factors. *The Journal of cell biology*, 75(2):606–616, 1977.

[18] Sally H Zigmond. Consequences of chemotactic peptide receptor modulation for leukocyte orientation. *The Journal of cell biology*, 88(3):644–647, 1981.

[19] DUSTIN W BREWER and S Pankavich. Computational methods for a one-dimensional plasma model with transport field. *SIAM Undergraduate Research Online*, 4:81–104, 2011.

[20] Youcef Saad and Martin H Schultz. Gmres: A generalized minimal residual algorithm for solving nonsymmetric linear systems. *SIAM Journal on scientific and statistical computing*, 7(3):856–869, 1986.

[21] Randall J LeVeque. *Finite volume methods for hyperbolic problems*, volume 31. Cambridge university press, 2002.

[22] Jonathan Istok. Groundwater modeling by the finite element method. 1989.

[23] I. Battiato and D. M. Tartakovsky. Applicability regimes for macroscopic models of reactive transport in porous media. *J. Contam. Hydrol.*, 120-121:18–26, 2011.

[24] H. Arunachalam, S. Onori, and I. Battiato. On veracity of macroscopic lithium-ion battery models. *J. Electrochem. Soc.*, 162(10):A1940–A1951, 2015.

[25] U. Hornung. *Homogenization and porous media*, volume 6. Springer, 2012.

[26] S. Whitaker. *The method of volume averaging*, volume 13. Springer, 2013.

[27] M. Schmuck and M. Z. Bazant. Homogenization of the Poisson-Nernst-Planck equations for ion transport in charged porous media. *SIAM J. Appl. Math.*, 75(3):1369–1401, 2015.

[28] S. Korneev and I. Battiato. Sequential homogenization of reactive transport in polydisperse porous media. *Multiscale Model. Simul*, 14(4):1301–1318, 2016.

[29] X. Zhang and D. M. Tartakovsky. Effective ion diffusion in charged nanoporous materials. *J. Electrochem. Soc.*, 164(4):E53–E61, 2017.

[30] A. Mikelić. An introduction to the homogenization modeling of non-Newtonian and electrokinetic flows in porous media. In A. Farina, A. Mikelić, and F. Rosso, editors, *New trends in non-Newtonian fluid mechanics and complex flows*, Lecture Notes in Mathematics. Springer, 2017.

[31] F. Boso and I. Battiato. Homogenizability conditions for multicomponent reactive transport. *Adv. Water Res.*, 62:254–265, 2013.

[32] M. Yousefzadeh and I. Battiato. Physics-based hybrid method for multiscale transport in porous media. *J. Comput. Phys.*, 341:320–338, 2017.

[33] X. Zhang, K. Urita, I. Moriguchi, and D. M. Tartakovsky. Design of nanoporous materials with optimal sorption capacity. *J. Appl. Phys.*, 117(24):244304, 2015.

[34] X. Zhang and D. M. Tartakovsky. Optimal design of nanoporous materials for electrochemical devices. *Appl. Phys. Lett.*, 110(14):143103, 2017.

[35] X. Lu, D. Zheng, T. Zhai, Z. Liu, Y. Huang, S. Xie, and Y. Tong. Facile synthesis of large-area manganese oxide nanorod arrays as a high-performance electrochemical supercapacitor. *Energy Environ. Sci.*, 4(8):2915–2921, 2011.

[36] D. Cheng, Y. Yang, Y. Luo, C. Fang, and J. Xiong. Growth of ultrathin mesoporous Ni-Mo oxide nanosheet arrays on Ni foam for high-performance supercapacitor electrodes. *Electrochim. Acta*, 176:1343–1351, 2015.

[37] A. González, E. Goikolea, J. A. Barrena, and R. Mysyk. Review on supercapacitors: Technologies and materials. *Renew. Sustainable Energy Rev.*, 58:1189–1206, 2016.

[38] V. Subramanian, S. C. Hall, P. H. Smith, and B. Rambabu. Mesoporous anhydrous RuO_2 as a supercapacitor electrode material. *Solid State Ion.*, 175(1):511–515, 2004.

[39] G. Limousin, J.-P. Gaudet, L. Charlet, S. Szenknect, V. Barthes, and M. Krimissa. Sorption isotherms: a review on physical bases, modeling and measurement. *Appl. Geochem.*, 22(2):249–275, 2007.

[40] W. Plazinski, W. Rudzinski, and A. Plazinska. Theoretical models of sorption kinetics including a surface reaction mechanism: a review. *Adv. Colloid Interface Sci.*, 152(1):2–13, 2009.

[41] A. Saltelli, M. Ratto, T. Andres, F. Campolongo, J. Cariboni, D. Gatelli, M. Saisana, and S. Tarantola. *Global Sensitivity Analysis: The Primer*. Wiley, Chichester, England, 2008.

[42] R. C. Smith. *Uncertainty Quantification: Theory, Implementation, and Applications*. Computational Science and Engineering. SIAM, Philadelphia, PA, 2014.

[43] T. Homma and A. Saltelli. Importance measures in global sensitivity analysis of nonlinear models. *Reliab. Eng. Syst. Safe.*, 52(1):1–17, 1996.

[44] I. M. Sobol'. Sensitivity estimates for nonlinear mathematical models. *Math. Model. Comput. Exp.*, 1:40, 1993. Matematicheskoe Modelirovanie 2, 112-118, 1990 (in Russian), translated in English (1993).

[45] B. Sudret. Global sensitivity analysis using polynomial chaos expansions. *Reliab. Eng. Syst. Safe.*, 93(7):964–979, 2008.

[46] B. M. Adams, L. E. Bauman, W. J. Bohnhoff, K. R. Dalbey, M. S. Ebeida, J. P. Eddy, M. S. Eldred, P. D. Houg, K. T. Hu, J. D. Jakeman, J. A. Stephens, L. P. Swiler, D. M. Vigil, and T. M. Wildey. *Dakota, A Multilevel Parallel Object-Oriented Framework for Design Optimization, Parameter Estimation, Uncertainty Quantification, and Sensitivity Analysis (SAND2014-4633)*. Sandia National Laboratory, version 6 edition, 2015.

[47] R. G. Ghanem and P. D. Spanos. *Stochastic Finite Elements: A Spectral Approach*. Dover, Mineola, NY, revised edition, 2003.

[48] D. Xiu. *Numerical Methods for Stochastic Computations: A Spectral Method Approach*. Princeton University Press, Princeton, NJ, 2010.

[49] O. P. Le Maître and O. M. Knio. *Spectral Methods for Uncertainty Quantification: With Applications to Computational Fluid Dynamics*. Springer, Berlin, Germany, 2010.

[50] Z. I. Botev, J. F. Grotowski, and D. P. Kroese. Kernel density estimation via diffusion. *Ann. Stat.*, 38(5):2916–2957, 2010.

[51] G. Severino, G. Dagan, and C. J. van Duijn. A note on transport of a pulse of nonlinearly reactive solute in a heterogeneous formation. *J. Comput. Geosci.*, 4:275–286, 2000.

[52] M. Ye, S. P. Neuman, Alberto Guadagnini, and D. M. Tartakovsky. Nonlocal and localized analyses of conditional mean transient flow in bounded, randomly heterogeneous porous media. *Water Resour. Res.*, 40:W05104, 2004.

[53] G. Lin, A. M. Tartakovsky, and D. M. Tartakovsky. Uncertainty quantification via random domain decomposition and probabilistic collocation on sparse grids. *J. Comput. Phys.*, 229(19):6995–7012, 2010.

[54] G. Severino, D. M. Tartakovsky, G. Srinivasan, and H. Viswanathan. Lagrangian models of reactive transport in heterogeneous porous media with uncertain properties. *Proc. R. Soc. A*, 468(2140):1154–1174, 2012.

[55] J. Guilleminot, C. Soize, and R. G. Ghanem. Stochastic representation for anisotropic permeability tensor random fields. *Int. J. Numer. Anal. Methods Geomech.*, 36(13):1592–1608, 2012.

[56] Daphne Koller and Nir Friedman. *Probabilistic graphical models: principles and techniques*. MIT press, 2009.

[57] Larry Wasserman. *All of statistics: a concise course in statistical inference*. Springer Science & Business Media, 2013.

[58] M Bishop Christopher. *PATTERN RECOGNITION AND MACHINE LEARNING.* Springer-Verlag New York, 2016.

[59] Murray Rosenblatt. Remarks on a multivariate transformation. *The annals of mathematical statistics*, 23(3):470–472, 1952.

[60] E Torre, S Marelli, P Embrechts, and B Sudret. A general framework for uncertainty quantification under non-gaussian input dependencies. *arXiv preprint arXiv:1709.08626*, 2017.

[61] Martin Meier-Schellersheim, Iain DC Fraser, and Frederick Klauschen. Multiscale modeling for biologists. *Wiley Interdisciplinary Reviews: Systems Biology and Medicine*, 1(1):4–14, 2009.

[62] Y Cheng, P Kekenes-Huskey, JE Hake, MJ Holst, JA McCammon, and AP Michailova. Multi-scale continuum modeling of biological processes: from molecular electro-diffusion to sub-cellular signaling transduction. *Computational science & discovery*, 5(1):015002, 2012.

[63] Tom NP Bosma, Jerald L Schnoor, Gosse Schraa, and Alexander JB Zehnder. Simulation model for biotransformation of xenobiotics and chemotaxis in soil columns. *Journal of Contaminant Hydrology*, 2(3):225–236, 1988.

[64] Nicholas Dudley Ward, Samuel Falle, and Mira Stone Olson. Modeling chemotactic waves in saturated porous media using adaptive mesh refinement. *Transport in porous media*, 89(3):487–504, 2011.

[65] Rebecca Tyson, LG Stern, and Randall J LeVeque. Fractional step methods applied to a chemotaxis model. *Journal of mathematical biology*, 41(5):455–475, 2000.

[66] Dirk Horstmann et al. From 1970 until present: the keller-segel model in chemotaxis and its consequences. 2003.

[67] Sara Vieira-Silva and Eduardo PC Rocha. The systemic imprint of growth and its uses in ecological (meta) genomics. *PLoS Genet*, 6(1):e1000808, 2010.

[68] Daniel T Gillespie. Exact stochastic simulation of coupled chemical reactions. *The journal of physical chemistry*, 81(25):2340–2361, 1977.

[69] Desmond J Higham. Modeling and simulating chemical reactions. *SIAM review*, 50(2):347–368, 2008.

[70] C. Bringedal, I. Berre, I. S. Pop, and F. A. Radu. Upscaling of nonisothermal reactive porous media flow under dominant péclet number: The effect of changing porosity. *Multiscale Model. Simul.*, 14(1):502–533, 2016.

[71] Dongbin Xiu and George Em Karniadakis. The wiener–askey polynomial chaos for stochastic differential equations. *SIAM journal on scientific computing*, 24(2):619–644, 2002.

[72] Isamu Moriguchi, Yuki Shono, Hirotoshi Yamada, and Tetsuichi Kudo. Colloidal crystal-derived nanoporous electrode materials of cut swnts-assembly and tio2/swnts nanocomposite. *The Journal of Physical Chemistry B*, 112(46):14560–14565, 2008.

[73] Yuh-Shan Ho and Gordon McKay. Pseudo-second order model for sorption processes. *Process biochemistry*, 34(5):451–465, 1999.

[74] Saeid Azizian. Kinetic models of sorption: a theoretical analysis. *Journal of colloid and Interface Science*, 276(1):47–52, 2004.

[75] Jacob Bear and Alexander H-D Cheng. *Modeling groundwater flow and contaminant transport*, volume 23. Springer Science & Business Media, 2010.

[76] Carl G Enfield, Curtis C Harlin, and Bert E Bledsoe. Comparison of five kinetic models for orthophosphate reactions in mineral soils. *Soil Science Society of America Journal*, 40(2):243–249, 1976.

[77] Cornelius J Van Duijn and Peter Knabner. Travelling waves in the transport of reactive solutes through porous media: Adsorption and binary ion exchangepart 1. *Transport in porous media*, 8(2):167–194, 1992.

[78] Walter J Weber, Paul M McGinley, and Lynn E Katz. Sorption phenomena in subsurface systems: concepts, models and effects on contaminant fate and transport. *Water Research*, 25(5):499–528, 1991.

[79] Grégoire Allaire, Robert Brizzi, Andro Mikelić, and Andrey Piatnitski. Two-scale expansion with drift approach to the taylor dispersion for reactive transport through porous media. *Chemical Engineering Science*, 65(7):2292–2300, 2010.

[80] Andrea Saltelli, Marco Ratto, Terry Andres, Francesca Campolongo, Jessica Cariboni, Debora Gatelli, Michaela Saisana, and Stefano Tarantola. *Global sensitivity analysis: the primer*. John Wiley & Sons, 2008.

[81] Bruce Dunn, Haresh Kamath, and Jean-Marie Tarascon. Electrical energy storage for the grid: a battery of choices. *Science*, 334(6058):928–935, 2011.

[82] Vinodkumar Etacheri, Rotem Marom, Ran Elazari, Gregory Salitra, and Doron Aurbach. Challenges in the development of advanced li-ion batteries: a review. *Energy & Environmental Science*, 4(9):3243–3262, 2011.

[83] Aiping Yu, Victor Chabot, and Jiujun Zhang. *Electrochemical supercapacitors for energy storage and delivery: fundamentals and applications*. CRC Press, 2013.

[84] Kamaljit Chowdhary and Paul Dupuis. Distinguishing and integrating aleatoric and epistemic variation in uncertainty quantification. *ESAIM: Mathematical Modelling and Numerical Analysis*, 47(3):635–662, 2013.

[85] Eric Joseph Hall and Markos A Katsoulakis. Robust information divergences for model-form uncertainty arising from sparse data in random pde. *arXiv preprint arXiv:1708.03718*, 2017.

[86] Kimoon Um, Xuan Zhang, Markos Katsoulakis, Petr Plechac, and Daniel M Tartakovsky. Global sensitivity analysis of multiscale properties of porous materials. *Journal of Applied Physics*, 123(7):075103, 2018.